J. Fluid Mech. (2002), *vol.* 452, *pp.* 199–229.
DOI: 10.1017/S0022112001006917 Printed in the United Kingdom

Transport enhancement mechanisms in open cavities

By MARC HORNER[1], GUY METCALFE[2], S. WIGGINS[3] AND J. M. OTTINO[1]†

[1]Department of Chemical Engineering, Northwestern University, Evanston, IL 60208, USA
[2]CSIRO Thermal and Fluids Engineering, Box 56 Graham Rd, Highett, Vic 3190, Australia
[3]Department of Mathematics, University of Bristol, Bristol BS8 1TW, UK

(Received 12 September 2000 and in revised form 3 August 2001)

By experiments and supporting computations we investigate two methods of transport enhancement in two-dimensional open cellular flows with inertia. First, we introduce a spatial dependence in the velocity field by periodic modulation of the shape of the wall driving the flow; this perturbs the steady-state streamlines in the direction perpendicular to the main flow. Second, we introduce a time dependence through transient acceleration–deceleration of a flat wall driving the flow; surprisingly, even though the streamline portrait changes very little during the transient, there is still significant transport enhancement. The range of Reynolds and Reynolds–Strouhal numbers studied is $7.7 \leqslant Re \leqslant 46.5$ and $0.52 \leqslant ReSr \leqslant 12.55$ in the spatially dependent mode and $12 \leqslant Re \leqslant 93$ and $0.26 \leqslant ReSr \leqslant 5.02$ in the time-dependent mode. The transport is described theoretically via lobe dynamics. For both modifications, a curve with one maximum characterizes the various transport enhancement measures when plotted as a function of the forcing frequency. A qualitative analysis suggests that the exchange first increases linearly with the forcing frequency and then decreases as $1/Sr$ for large frequencies.

1. Introduction

Two-dimensional flow in cavities, wedges and indentations, around corners and steps, and over obstructions has received considerable attention in the literature (see, for example, Shankar & Deshpande 2000 and Higdon 1985). An important feature of this class of flows, often referred to as cellular flows, is the presence of limiting streamlines – separatrices – which prohibit direct fluid exchange between the recirculating flow region and the surrounding fluid when the flow is steady. Molecular diffusion is the only transport mechanism across a separatrix.

Separatrices hinder transport. This is especially important in small-scale flows. Examples of cellular flows where there is interest in the suppression or enhancement of transport rates are wide-ranging, including the cleansing of rough surfaces (Tighe & Middleman 1985), various types of electrochemical reaction engineering applications (Alkire & Verhoff 1994), the understanding of pitting corrosion mechanisms (Frankel 1998), transport in or around printed circuit boards (Meinders, Meer & Hanjalic 1998), and efficient transport to cells in perfusion bioreactors (Horner *et al.* 1998).

† Author to whom correspondence should be addressed: e-mail ottino@chem-eng.northwestern.edu

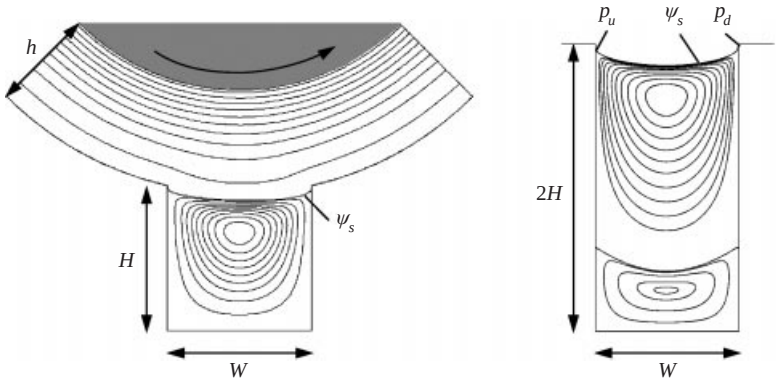

FIGURE 1. Experimental realization of the open cavity flow. The flow in the channel is driven by a cylinder. We consider cavity aspect ratios ($= W/H$) of either 1 or 0.5. Examples obtained using the computational methods described in § 2. ($Re = 46.5$)

In what ways can transport into a cellular flow be enhanced? We investigate two different routes: geometrically modifying the boundary driving the flow and making the flow time-dependent. In either case, these modifications destabilize one of the wall attachment points of the separatrix, allowing fluid exchange between the cavity and channel. We analyse the transport enhancement in terms of the turnstile-lobe transport mechanism (Mackay, Meiss & Percival 1984; Rom-Kedar, Leonard & Wiggins 1990). This mechanism is so-named because flow perturbations lead to the formation of lobes that transfer material across the separatrix through what looks like a turnstile. We examine the effect of both the frequency and the amplitude of periodic perturbations on the transport enhancement. The system of interest is the open cavity flow (figure 1). As we shall see, this geometry is a particularly clear illustration of the turnstile-lobe transport mechanism because a single lobe pair forms at only one place in most of the experiments.

There is only a handful of studies of chaotic mixing in open cavities; they are primarily computational. Jana & Ottino (1992) show a single computation illustrating the removal of material from an open cavity by the oscillating motion of an impinging jet above the cavity mouth. Howes & Shardlow (1997) examine the cleaning of a series of open cavities in a channel with a pulsatile inlet flow. They show that the relative amplitude of the forcing flow must increase as the Reynolds number increases to achieve full penetration of particles into the channel ($Re \leqslant 120$, $0.15 < Sr < 0.25$, where Sr is Strouhal number). Fang, Nicolaou & Cleaver (1999) consider fluid transfer for accelerating flow past an open cavity for Reynolds numbers ranging from 50 to 400. At sufficiently high Reynolds numbers, the introduction of obstacles upstream of an open cavity creates oscillations in the flow that induce fluid exchange (Garrison & Rogers 1994; Shehata *et al.* 1999); even the presence of multiple cavities in series can enhance transport (Ghaddar *et al.* 1986). Other relevant geometries where the effects of chaotic mixing have also been examined include baffled channels (Roberts & Mackley 1995), separation bubbles (Ghosh, Leonard & Wiggins 1998), and Rayleigh–Bénard flow (Solomon, Thomas & Warner 1998). Solomon *et al.* (1998) observed experimentally that transport increases as the amplitude of the forcing increases.

Recognizing that the flux of material into an open flow typically increases linearly when the forcing frequency is small, and decreases exponentially as the forcing

frequency goes to infinity, Rom-Kedar & Poje (1999) recently suggested that a universal curve with at least one maximum qualitatively describes the material exchange in the region of a perturbed hyperbolic saddle. Their analysis is specific to flows containing hyperbolic saddles, however. This paper addresses experimentally the frequency-dependence issue for *parabolic*-type saddles, in a quantitative manner, and over a broad range of forcing frequencies. Experimental results compare well to a computational model of the transiently forced system.

The rest of this paper is organized as follows: in § 2 we introduce the time-dependent and spatially dependent flows as well as the numerical solution methods. Section 3 gives the relevant theory from lobe dynamics for describing turnstile-lobe transport. In § 4 we describe the experimental apparatus and details of the experimental protocol, and in § 5 we give a detailed description of the observed transport into an open cellular flow. The results for the spatial modification are summarized in § 6 and the results for the time-dependent modification are presented in § 7. The conclusions are summarized in § 8.

2. The open cavity flow

The basic open cavity system is shown in figure 1. The top wall moves from left to right in every figure in this paper. Therefore, we refer to the left-hand cavity wall as the upstream side and the right-hand cavity wall as the downstream side. A separatrix ψ_s separates the channel and cavity streamlines. The separatrix attaches to the sidewalls of the cavity, near the cavity mouth, at parabolic points: p_u is the upstream parabolic point and p_d is the downstream parabolic point. While we recognize the presence of an infinite series of corner (Moffatt) eddies in each corner of the cavity, we do not consider the transport associated with these eddies owing to their small size and circulation strength relative to the main cavity flow.

In the steady state, the presence of the separatrix means that there is no fluid exchange between the cavity and the channel. In order to enhance transport, we explore two different types of (periodic) time-dependent modifications: either we make the shear flow in the channel vary in time (T-mode) or we modify the boundary driving the flow such that there is spatial variation in the boundary geometry (S_N-mode). In either case, perturbations give rise to direct fluid exchange between the two environments through the turnstile-lobe transport mechanism; we discuss this mechanism in more detail in the next section. The net effect of the flow modifications is the destabilization of the downstream parabolic attachment point of the separatrix, leading to the formation of lobes (figure 2). Lobes are the fundamental building blocks for transport enhancement. Repeated operation creates a mixing zone in the cavity in which the flow is chaotic. KAM tori isolate a region within the mixing zone where the flow is regular.

In the T-mode, the (smooth) driving wall accelerates from rest to a maximum speed and then immediately decelerates, at the same rate, back to zero (figure 3). The change in the velocity field for this type of flow is primarily tangent to the direction of wall motion. In the S_N-mode, we create flow disturbances that are primarily perpendicular to the direction of the shear flow by attaching N cylindrical rods to the driving wall (figure 4). In a subset of the S_N-mode experiments, when $N = 10$, we also attach a thin rubber sheet on top of the rods to approximate a sinusoidal variation in the boundary geometry (figure 4*b*). The speed of the driving wall in the S_N-mode is constant.

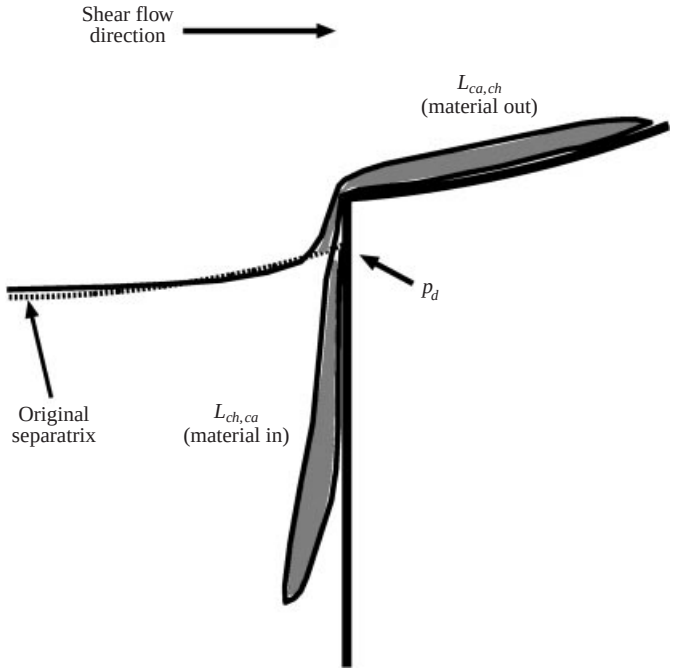

FIGURE 2. Separation of the stable and unstable manifolds that make up the separatrix results in the formation of lobes. $L_{ch,ca}$ represents *channel* ('*ch*') material that is entrained in the *cavity* ('*ca*') and vice versa for $L_{ca,ch}$. The area of $L_{ch,ca}$ equals that of $L_{ca,ch}$ for incompressible flows. The dashed line represents the initial (final) position of the dye-line before (after) the perturbation and p_d is the downstream parabolic wall-attachment point.

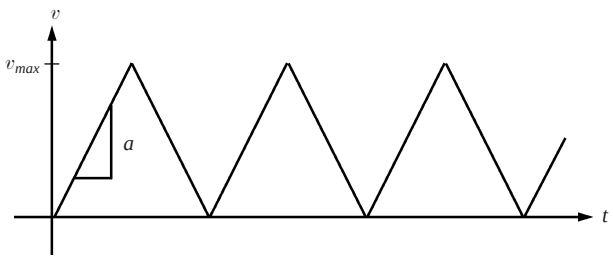

FIGURE 3. The velocity profile for the transient modification (T-mode) has a sawtooth or triangular shape. The period of each sawtooth cycle is $2v_{max}/a$.

The system is described in terms of the Navier–Stokes equations,

$$\rho\left(\frac{\partial \boldsymbol{u}}{\partial t} + \boldsymbol{u}\cdot\nabla\boldsymbol{u}\right) = -\nabla P + \mu\nabla^2\boldsymbol{u}, \tag{2.1}$$

and we assume that the fluid is incompressible, i.e. $\nabla\cdot\boldsymbol{u} = 0$. The characteristic length scale and velocity are the cavity width W and the maximum cylinder velocity v_{max}. The forcing period T is used to scale time. Substituting

$$t \to \frac{t}{T}, \qquad x \to \frac{x}{W}, \qquad u \to \frac{u}{v_{max}}, \tag{2.2}$$

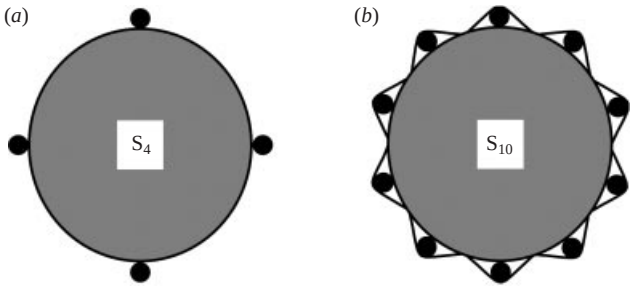

FIGURE 4. Examples of S_N-mode flows. The number of rods varies between 1 and 10. (*b*) An outer wall is also attached on top of the rods and cylinder when there are 10 rods present, a modification designed to approximate a smooth, sinusoidal variation in the wall geometry. The boundary motion is constant ($= v_{max}$) in the S_N-mode.

into equation (2.1) gives

$$Re\left(Sr\frac{\partial \boldsymbol{u}}{\partial t} + \boldsymbol{u}\cdot\nabla\boldsymbol{u}\right) = -\nabla P + \nabla^2\boldsymbol{u}, \tag{2.3}$$

where we have used a viscous scaling for the pressure term. Re is the Reynolds number

$$Re = \frac{v_{max}W}{\nu}, \tag{2.4}$$

where $\nu = \mu/\rho$ is the kinematic viscosity of the fluid, and Sr is the Strouhal number

$$Sr = \frac{W}{v_{max}T}. \tag{2.5}$$

The Reynolds number is the ratio of the viscous time scale (W^2/ν) to the convective time scale (W/v_{max}) and the Strouhal number is the ratio of the convective time scale to the characteristic time scale of the forcing (T). The expressions for T in the T-mode and in the S_N-mode are different; we consider this issue in § 6 and § 7. The consequence of forcing the system externally is that two independent parameters describe the inertial terms in equation (2.3): Re and its product with Sr

$$ReSr = \frac{W^2}{\nu T}. \tag{2.6}$$

We characterize all results in terms of Re and $ReSr$. Variations in Re corresponds to changing the amplitude of the forcing, while varying $ReSr$ corresponds to changing the forcing frequency.

We use the finite element package FIDAP (version 7.52) for the numerical solution of the equations of motion. We solve the two-dimensional form of equation (2.3) with no-slip boundaries, utilizing a backward Euler approximation of the time derivatives in the T-mode simulations and a pseudo-steady approximation of the velocity field for the S_N-mode simulations. The pseudo-steady approach for the S_N-mode eliminates the need for a moving mesh as rods pass by the cavity. We advect passive tracers in the flows using either a fourth-order Runga–Kutta scheme with variable time step or FIDAP's internal advection routine.

Consider now the change in the flow patterns during a single perturbation cycle. Figure 5 shows the instantaneous streamlines for the S_{10} modification. Marked changes in the velocity field occur as waves pass over the cavity: channel streamlines penetrate well into the cavity, and vice versa, and there is clear overlapping of streamline

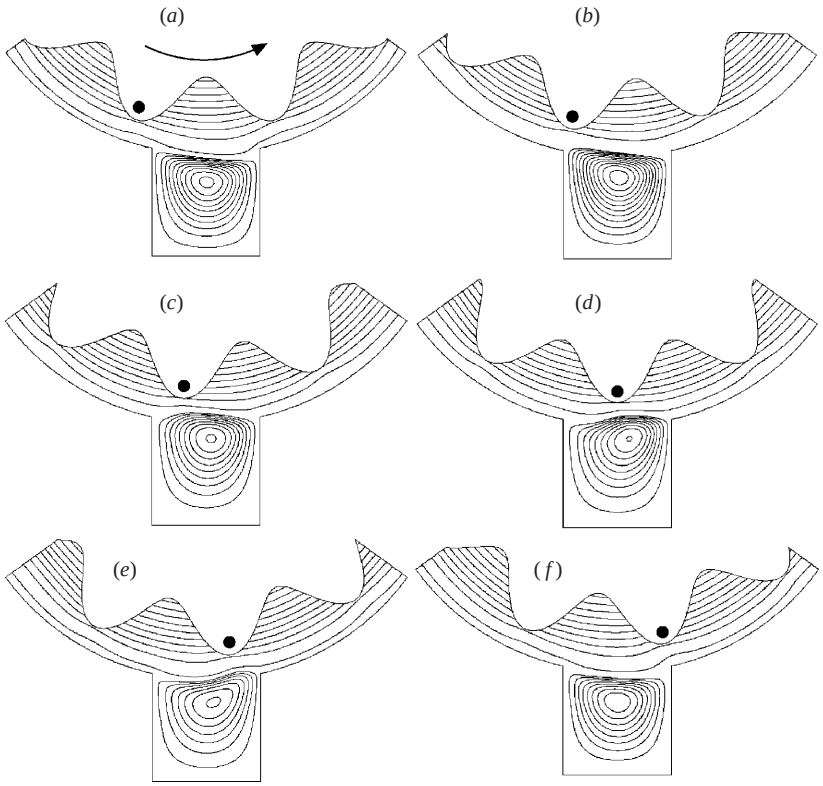

FIGURE 5. Time-series illustrating the instantaneous streamline pattern for the S_{10} flow past an open cavity. The dot highlights the position of a specific wave as it passes over the cavity; the wall displacement is 1/6th of a wavelength between frames ($Re = 46.5$, $ReSr = 47.0$, $W/H = 1.0$).

portraits at subsequent times. This immediately suggests that particle trajectories in the cavity are chaotic. Figure 6 shows a time series of the instantaneous streamlines for the T-mode. The cellular flow pattern is only slightly asymmetric, showing similarity to that for steady motion at all times. A close-up of the separatrix region (figure 7) shows that the instantaneous separatrix changes position only slightly during a single flow cycle. Nonetheless, we shall show that transient perturbations produce significant transport.

3. Lobe dynamics

In this section we discuss a few concepts from dynamical systems theory that will be crucial for understanding the transport mechanism associated with the open cavity flow. Transport in aperiodic flows is described in Haller & Poje (1998) and Miller *et al.* (1997). The presentation below is based on Malhotra & Wiggins (1998).

At each instant of time there is a point on the upstream vertical wall of the cavity where fluid separates from the wall, denoted $p_u(t)$. This point moves periodically in time with the period of the flow. In the language of dynamical systems theory, this is a *saddle-type parabolic trajectory*. If we consider the stroboscopic (Poincaré) map associated with the flow, then this point is a parabolic fixed point for the Poincaré map (which means that the two eigenvalues of the matrix associated with the linearization of the Poincaré map both lie on the unit circle). Despite this fact, this point exhibits

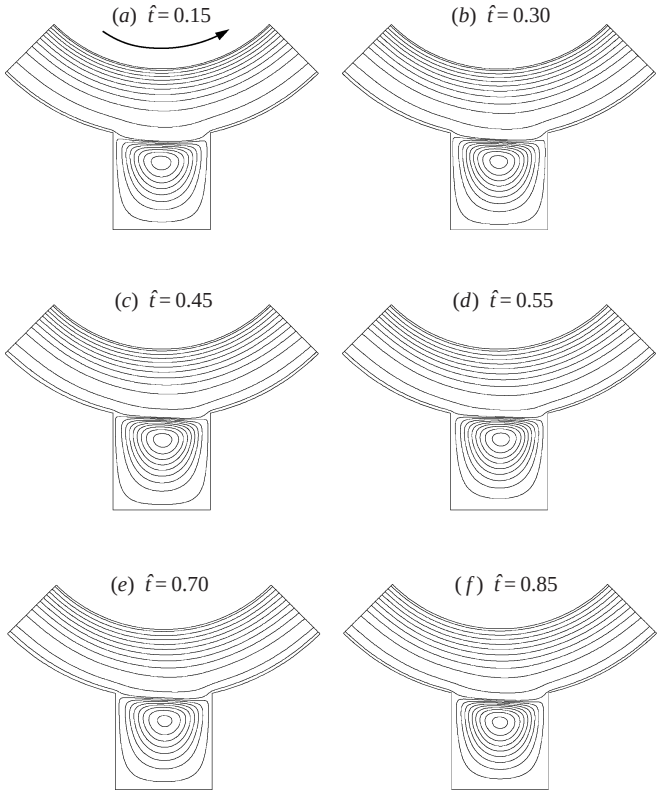

FIGURE 6. Instantaneous streamlines for one cycle of the T-mode. $\hat{t}$ is the fraction of one sawtooth cycle, i.e. $\hat{t} = t/(2v_{max}/a)$ ($Re = 92.9$, $ReSr = 1.26$, $W/H = 1.0$).

the flow topology of a saddle point. Similarly, there is a point on the downstream vertical wall of the cavity where fluid impinges on the wall and separates, with some moving upward and some moving downward. This point, denoted $p_d(t)$, is also a saddle-type parabolic trajectory.

In dynamical systems theory, *hyperbolic* saddle points possess stable and unstable manifolds, and these invariant manifolds form the template in the flow on which turnstiles and lobes are constructed. In recent years there has been progress in the development of theorems for stable and unstable manifolds of saddle-type parabolic points, see McGehee (1973), Casasayas, Fontich & Nunes (1992), Yuster & Hackborn (1997) and Fontich (1999). These results allow us to conclude that $p_u(t)$ has an unstable manifold, denoted $W^u(p_u(t))$, likewise $p_d(t)$ has a stable manifold, denoted $W^s(p_d(t))$.

Manifolds are *invariant curves*, i.e. particle trajectories that start on these curves must stay on them for all time. This is the mathematical statement of the fact that they are material curves. Hence, they are barriers to transport in the sense that no particle trajectories can cross them. Another property of invariant manifolds is that particle trajectories that start on $W^s(p_d(t))$ approach $p_d(t)$ as $t \to \infty$, likewise trajectories that start on $W^u(p_u(t))$ approach $p_u(t)$ as $t \to -\infty$. When the flow is steady, $W^u(p_u)$ and $W^s(p_d)$ coincide to create the separatrix (e.g. ψ_s in figure 1). When the system is forced appropriately, $W^u(p_u(t))$ and $W^s(p_d(t))$ separate to create a heteroclinic tangle (figure 8). We now define regions bounded by pieces of stable

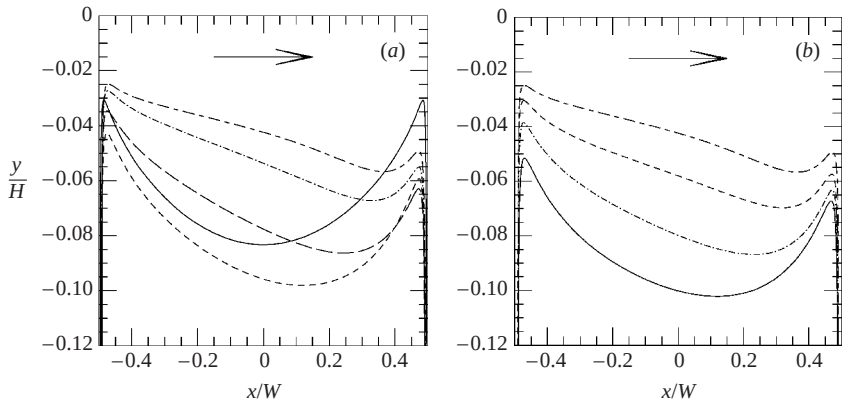

FIGURE 7. We track the change in position of a streamline passing very near the separatrix (from below). The origin is located at the centre of the cavity mouth, and note that the scale of the y-axis is exaggerated. (a) Acceleration phase of the flow: $\hat{t} = 0\,\mathrm{s}$ (——), $\hat{t} = 0.15\,\mathrm{s}$ (- - -), $\hat{t} = 0.3\,\mathrm{s}$ (– – –), $\hat{t} = 0.45\,\mathrm{s}$ (-·-·-·-), and $\hat{t} = 0.55\,\mathrm{s}$ (– - – - –); and (b) deceleration phase of the flow cycle: $\hat{t} = 0.55\,\mathrm{s}$ (– - – - –), $\hat{t} = 0.7\,\mathrm{s}$ (- - -), $\hat{t} = 0.85\,\mathrm{s}$ (-·-·-·-), and $\hat{t} = 0.975\,\mathrm{s}$ (——). See figure 6 for simulation conditions.

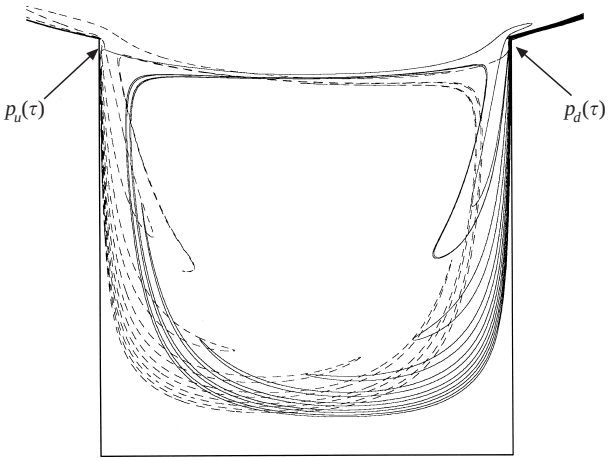

FIGURE 8. Portions of the stable (- - -) and unstable (—) manifolds derived from the computational model for the T-mode. The asymmetry of the manifold structure is due to the presence of inertia (T-mode: $Re = 46.5$, $ReSr = 1.26$, $W/H = 1.0$).

and unstable manifolds, called *lobes*, which completely determine transport between the cavity and the channel.

At a fixed time $t = \tau$ consider a point $p \in W^s(p_d(\tau)) \cap W^u(p_u(\tau))$. Let $[p_d(\tau), p]$ denote the segment of $W^s(p_d(\tau))$ connecting $p_d(\tau)$ to p and let $[p_u(\tau), p]$ denote the segment of $W^u(p_u(\tau))$ connecting $p_u(\tau)$ to p. Then p is said to be a *primary intersection point* (pip) if $[p_d(\tau), p]$ and $[p_u(\tau), p]$ intersect only at p (see figure 9).

With this definition we can now define a lobe. Suppose p and q are two pips such that there are no other pips on the segments of $W^s(p_d(\tau))$ and $W^u(p_u(\tau))$ that connect p and q. Then the region at the time $t = \tau$ bounded by the segments of $W^s(p_d(\tau))$ and $W^u(p_u(\tau))$ that connect p and q is called a *lobe*, which we denote by L^{pq} (see figure 9).

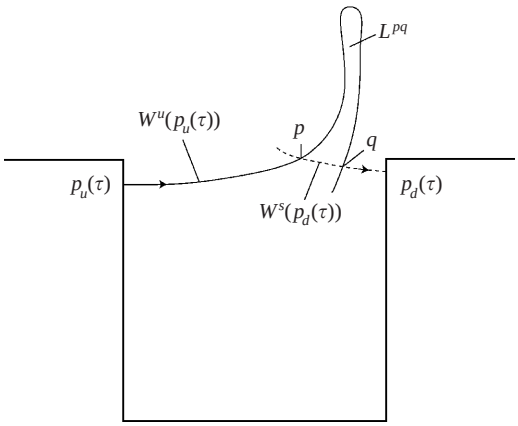

FIGURE 9. A lobe, L^{pq}, at a fixed time τ. Here the superscript 'pq' is used to explicitly denote the fact that this lobe is defined by segments of the stable and unstable manifolds that intersect at the primary intersection points p and q. We only show enough of the length of the manifolds to illustrate one lobe. The lobe shape is also distorted with respect to its true shape for clarity.

The time evolution of lobes can be deduced from two rules:

Rule 1: Maintenance of order under time evolution. Since at any fixed time $t = \tau$ the curves $W^u(p_u(\tau))$ and $W^s(p_d(\tau))$ are one-dimensional, points on them can be ordered. We define an ordering of points on $W^s(p_d(\tau))$ as follows. For any two points $q_\tau, \bar{q}_\tau \in W^s(p_d(\tau))$ we say that $q_\tau <_s \bar{q}_\tau$ if q_τ is closer than $\bar{q}_\tau$ to $p_d(\tau)$ in the sense of arclength along the curve $W^s(p_d(\tau))$. A similar type of ordering applies to points on $W^u(p_u(\tau))$. Let $x(t, t_0, x_0)$ denote the fluid particle trajectory that passes through the point x_0 at time $t = t_0$. Then $x(t, \tau, q_\tau) \equiv q_{\tau+t}, x(t, \tau, \bar{q}_\tau) \equiv \bar{q}_{\tau+t}$ denote points at time $\tau + t$ that are the time evolution of the points $q_\tau, \bar{q}_\tau$. By invariance, these points are also in $W^s(p_d(\tau + t))$. Moreover, we have $q_{\tau+t} <_s \bar{q}_{\tau+t}$. This follows from uniqueness of solutions, otherwise there would be an intermediate time on which the trajectories passed through each other.

Rule 2: Invariance of intersections. If the stable and unstable manifolds of a trajectory (or two different trajectories) intersect at a fixed time, then they intersect for all time. This simply follows from the fact that the manifolds are invariant for all time.

Let $\{t_n\}_{n=0}^N$ be a monotonically increasing sequence of times, where we could have $N = \infty$. These are the times at which we observe the flow. If $x(t, t_0, x_0)$ denotes the fluid particle trajectory passing through the point x_0 at $t = t_0$ then, for each $n \in \{0, \ldots, N\}$, we have the map

$$f_n : x_n \mapsto f_n(x_n) \equiv x(t_{n+1}, t_n, x_n) = x_{n+1}, \tag{3.1}$$

which is just the mapping of points under the flow from time t_n to t_{n+1}. The inverse map is given by

$$f_n^{-1} : x_{n+1} \mapsto f_n^{-1}(x_{n+1}) \equiv x(t_n, t_{n+1}, x_{n+1}) = x_n. \tag{3.2}$$

At time $t = t_n$ choose a point q_n on $W^u(p_u(t_n)) \cap W^s(p_d(t_n))$. Let $U[p_u(t_n), q_n]$ denote the segment of $W^u(p_u(t_n))$ beginning at $p_u(t_n)$ and ending at q_n and let $S[p_d(t_n), q_n]$ denote the segment of $W^s(p_d(t_n))$ beginning at $p_d(t_n)$ and ending at q_n. The points in the sequence $\{q_n\}$ are chosen such that

$$q_n <_s f_n^{-1}(q_{n+1}), \quad \forall n \in Z, \tag{3.3}$$

and are referred to as *boundary intersection points* (bips). The sequence $\{q_n\}$ can

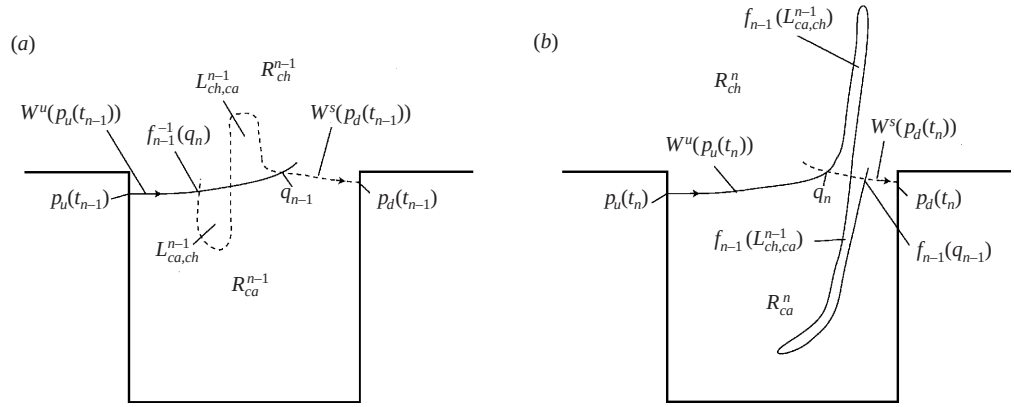

FIGURE 10. The turnstile-lobe transport mechanism. The dashed line is the stable manifold of p_d and the solid line is the unstable manifold of p_u. (*a*) $t = t_{n-1}$, (*b*) $t = t_n$.

always be chosen to satisfy this constraint as a result of the fact that all points in $W^u(p_u(t)) \cap W^s(p_d(t))$ at a given time will have moved closer to $W^s(p_d(t))$ – closer in the sense of distance in arclength from $p_d(t)$ – at any later time. This sequence of bips is used to construct a sequence of time-dependent boundaries and families of special lobes called 'turnstiles'.

$\mathscr{B}_n \equiv U[p_u(t_n), q_n] \cup S[p_d(t_n), q_n]$ is a curve at time t_n joining $W^u(p_u(t_n))$ and $W^s(p_d(t_n))$. Locally, this curve separates the flow into two regions, which we denote by R^n_{ca} and R^n_{ch} (here the superscript on the regions indicates that they vary as t_n varies; the subscript '*ca*' denotes cavity and the subscript '*ch*' denotes channel). We are concerned with transport across this family of curves $\{\mathscr{B}_n\}_{n=0}^N$ at the sequence of times $\{t_n\}_{n=0}^N$ under the dynamics generated by the sequence of maps $\{f_n\}_{n=0}^N$.

Consider the point $f^{-1}_{n-1}(q_n) \in W^u(p_u(t_{n-1})) \cap W^s(p_d(t_{n-1}))$ for an arbitrary time $t = t_{n-1}$ (by the choice of the sequence $\{q_n\}$, we have $q_{n-1} <_s f^{-1}_{n-1}(q_n)$). There exists one pip between $f^{-1}_{n-1}(q_n)$ and q_{n-1}. This pip, along with $f^{-1}_{n-1}(q_n)$ and q_{n-1}, defines two lobes at time $t = t_{n-1}$; one in R^{n-1}_{ca}, denoted by $L^n_{ca,ch}$, and one in R^{n-1}_{ch}, denoted by $L^{n-1}_{ch,ca}$.

The lobes $L^n_{ca,ch} \cup L^{n-1}_{ch,ca}$ are called the *turnstile lobes associated with the boundary* $\mathscr{B}_{n-1}$ *at the time* $t = t_{n-1}$. The turnstile lobes are important because they mediate transport across the boundary $\mathscr{B}_{n-1}$. In fact, by applying the two rules stated earlier we easily conclude that $f_{n-1}(L^n_{ca,ch}) \subset R^n_{ch}, f_{n-1}(L^{n-1}_{ch,ca}) \subset R^n_{ca}$. Moreover, the only points that move from R^{n-1}_{ca} (resp. R^{n-1}_{ch}) into R^n_{ch} (resp. R^n_{ca}) under the action of f_{n-1} by crossing $\mathscr{B}_{n-1}$ are those that are in $L^n_{ca,ch}$ (resp. $L^{n-1}_{ch,ca}$). The turnstile construction and the time evolution of the turnstiles is shown in figure 10.

Let A denote an arbitrary region and denote the area of A by $\mu(A)$. The *instantaneous flux* from R^{n-1}_{ca} into R^n_{ch} across $\mathscr{B}_n$ is given by

$$\phi^{n-1}_{ca,ch} = \frac{1}{t_n - t_{n-1}} \mu(L^n_{ca,ch}). \tag{3.4}$$

Similarly, the *instantaneous flux* from R^{n-1}_{ch} into R^n_{ca} across $\mathscr{B}_n$ is given by

$$\phi^{n-1}_{ch,ca} = \frac{1}{t_n - t_{n-1}} \mu(L^{n-1}_{ch,ca}). \tag{3.5}$$

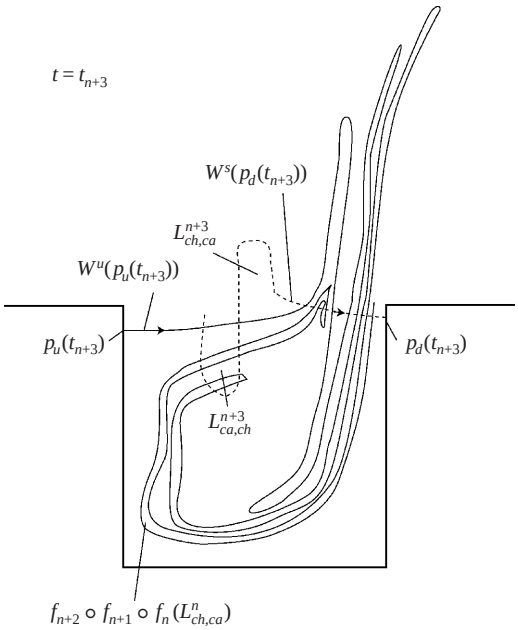

FIGURE 11. An illustration of global transport resulting from the evolution of the turnstile lobe entering the cavity intersecting the turnstile lobe leaving the cavity at a later time.

Note that if $\mathscr{B}_{n-1} = \mathscr{B}_n$ (as would be the case for a time-periodic flow), then $\phi^{n-1}_{ca,ch} = \phi^{n-1}_{ch,ca}$. Otherwise, even if the flow is incompressible, the boundaries would move between time intervals so these two fluxes need not be equal. The fluxes given above characterize the fluid exiting the cavity and entering the channel, and vice versa, during a single flow cycle. This aspect of transport is referred to as 'local'.

It is possible for fluid to enter the cavity from the channel and then re-enter the channel at a later time. This process is also completely determined by the turnstiles and lobe dynamics. As we argued earlier, fluid can only enter the channel between time t_n and time t_{n+1} through the turnstile lobe $L^n_{ch,ca}$. Similarly, fluid can only exit the cavity between time t_n and time t_{n+1} through the turnstile lobe $L^n_{ca,ch}$. Therefore, the only way for fluid to enter the cavity and then to exit the cavity at a later time is for the lobe $L^n_{ch,ca}$ to evolve in time in such a way that at a later time it intersects $L^m_{ca,ch}$, $m > n$. More precisely, we would have $f_{n+k-1} \circ f_{n+k-2} \circ \cdots \circ f_{n+1} \circ f_n(L^n_{ch,ca})$ intersecting $L^{n+k}_{ca,ch}$ ('$\circ$' denotes a composition of the mappings). We illustrate this in figure 11 for $k = 3$. This describes a 'global' transport process. Nevertheless, the global transport is still mediated by the time evolution of the turnstile lobes (see Rom-Kedar *et al.* 1990 for a discussion). This further illustrates the fact that the lobes form a geometrical template on which transport occurs. Spatially, this template can be very complicated. However, invariance of the manifolds, and the order property of trajectories on the manifolds, provide a temporal order that makes understanding the transport relatively easy.

4. Experimental description

The experimental apparatus consists of a mount table for the alignment and support of the motor and aluminium cylinder (figure 12*a*), and the dye advection chamber (figure 12*b*). The rotating cylinder drives the flow in the channel. The dye advection

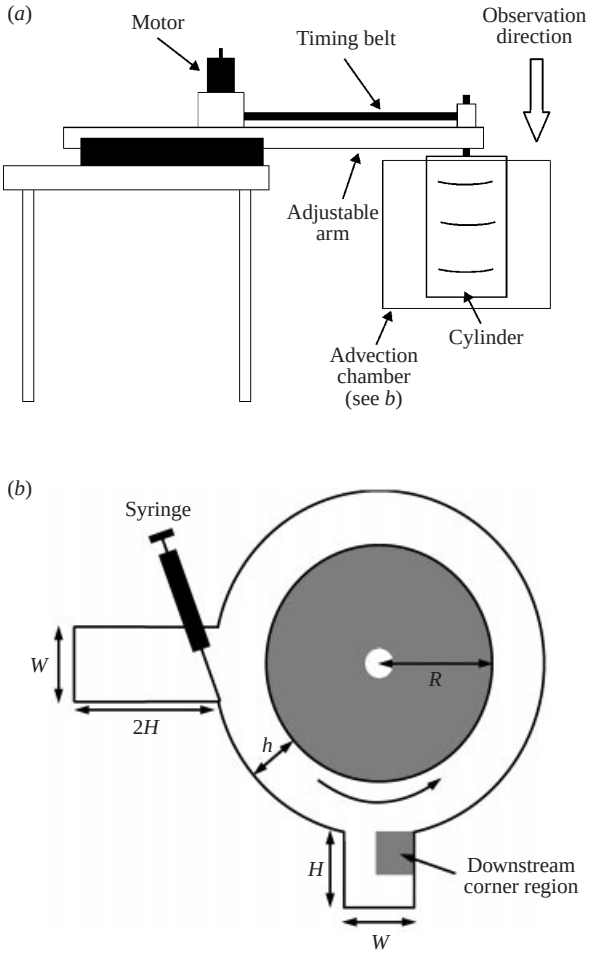

FIGURE 12. (*a*) Side view of the experimental set-up. The mount table supports the computer-controlled stepper motor and the suspending arm. The aluminium cylinder which drives the flow in the channel is attached to the end of the suspending arm with the axis of rotation aligned along the height of the cylinder. (*b*) Top view of the dye advection chamber. The aluminium cylinder is centred in the dye advection chamber by adjusting the suspending arm. The shaded region in the cavity highlights the 'downstream corner' of the cavity – the region of lobe formation ($W = 4.445$ cm, $H = 4.445$ cm, $R = 6.985$ cm, $h = 3.175$ cm).

chamber has a circular shape with four equally spaced cavities of varying size and shape, only two of which are shown. The four arcs making up the flow channel are cut from a 10.16 cm i.d. $\times$ 0.64 cm thick Plexiglas pipe and the individual cavity walls are cut from a separate sheet of Plexiglas of the same thickness. The channel and cavity walls are 17 cm high.

The aluminium cylinder is circular with a 6.99 cm o.d. and is 15 cm high. An aluminium arm suspends the cylinder 2 cm above the bottom of the dye advection chamber. The arm can be moved horizontally so as to centre the cylinder in the advection chamber. We measure the width of the channel at various points around the cylinder circumference using a micrometer (accurate to 10 μm). To level the cylinder and advection chamber, we use a digital level accurate to 1/10th of a degree. The

stepper-motor controller is programmable, allowing control of acceleration, velocity, and displacement of the cylinder.

In the S_N experiments of figure 4(*a*), we glue 1, 2, 4, or 10 equally spaced cylindrical aluminium rods (1.27 cm o.d.) to a 0.48 cm thick Buna-N rubber backing. These rods span the entire height of the aluminium cylinder. In the S_{10} experiments, we also glue another 0.16 cm thick rubber sheet to the rods and backing (figure 4*b*) to approximate a sinusoidal variation in the boundary geometry. For the S_{10} experiments, the average error in the rod spacing is 0.25% with a maximum spacing error of 0.6% (errors reported with respect to the perfect arrangement with equal distance between rods).

We use glycerin as the test fluid. To access the desired Reynolds and Reynolds–Strouhal number ranges, we increase the water content of the glycerin to either 1.25% by mass ($\rho = 1.260\,\mathrm{g\,cm^{-3}}$, $\mu = 9.57\,\mathrm{P}$ at $\mathrm{T} = 22.5^{\circ}\mathrm{C}$ (Miner & Dalton 1953)) or to 10% by mass $\rho = 1.236\,\mathrm{g\,cm^{-3}}$, $\mu = 1.95\,\mathrm{P}$ at $\mathrm{T} = 22.5\,^{\circ}\mathrm{C}$). We measure the viscosity of the glycerin before and after water addition using a Bohlin VOR Rheometer. To make the experiments effectively two-dimensional, we create a slip layer by first placing a high-density, low-viscosity vacuum pump oil (FOMBLIN® YL-VAC 06/6 perfluouropolyether) in the bottom of the chamber. The viscosity and density of the oil are 1.2 cP (25 °C) and $1.88\,\mathrm{g\,cm^{-3}}$ (25 °C), respectively. We add enough oil to cover about 2 cm of the base of the aluminium cylinder. The remaining chamber space is filled with the glycerin/water solution.

Fluorescent dye (Sigma F-6377) mixed with the glycerin marks fluid elements. Owing to the low concentration of the dye ($\approx 0.01\%$ by weight), changes in density and viscosity of the tracer fluid are negligible. We also assume that the dye solution is completely miscible in the test fluid, i.e. the dye solution acts as a passive tracer. We test the neutral buoyancy of the dye solution before each experiment by adjusting its water content until a dyed blob maintains its vertical position in a beaker of the working glycerin solution for 10–15 minutes. During an experiment, we use a syringe to continuously inject fluorescent dye into the system. The dye injection point is along the channel wall a few centimetres below the fluid surface and well upstream of the cavity of interest. This positioning minimizes any disturbances that might be advected downstream. Two UV lamps (360 nm) positioned on either side of the cavity illuminate the dyed fluid elements.

As the experiments are well outside the Stokes regime, we take care to test that the flow is effectively two-dimensional. The geometry of our open cavity flow apparatus is simply a modified Taylor–Couette flow geometry. The critical Taylor number for the onset of three-dimensional flow in our device is 2800 (Recktenwald, Lücke & Müller 1993), with a Reynolds number of 493. This value is considerably higher than the maximum Reynolds number studied experimentally. As another test, we inject multiple dye-lines at different heights in the chamber during the same experiment. No differences in lobe size or area coverage are observed during these tests for the range of *Re* and *ReSr* studied. Further, we observe motion of the dye in the vertical direction only for Reynolds numbers above 150. Below this value, dyed material is confined to a vertical region that is less than twice the needle diameter (0.16 cm).

Digital 8-bit greyscale images of the cavity are taken using a Kodak Megaplus 1.4 camera containing a 1340×1038 CCD detector. We use a NIKKOR 200 mm 1 : 4 lens with yellow and UV filters attached. The direction of observation is from above the cavity, i.e. the camera aims down through the air/glycerin interface. We acquire an image once per sawtooth cycle in the T-mode and once per revolution in the S_N-mode. We analyse the experimental images using the Khoros 2.2 digital image processing package. We determine the fractional area coverage of the cavity with dye,

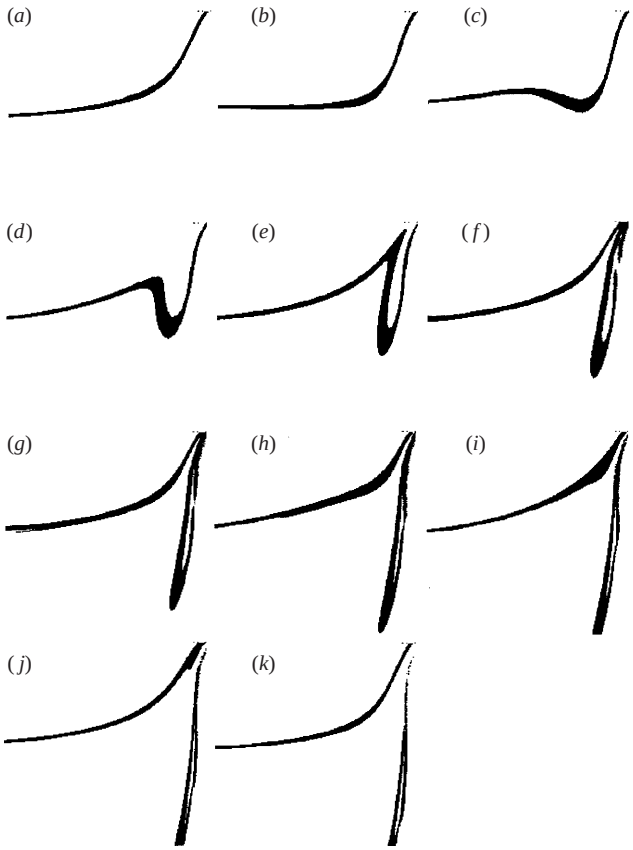

FIGURE 13. Experimental images of the downstream corner of the cavity showing one full cycle of the turnstile-lobe transport mechanism. The dye-line is pulled into the flow channel during lobe formation and returns to its initial position at the end of the flow cycle. One of the strengths of the open cavity geometry is that only one lobe pair forms per perturbation, greatly simplifying visualization and transport analysis.

and the size of a single lobe, using standard image analysis techniques. An important experimental issue should be mentioned: because of the circular flow channel, part of the dye exiting the cavity eventually returns to enter the cavity again (see figure 12). This means that new lobes steadily become filled with dye during an experiment. Therefore, we mask out the lobe interiors before determining the area coverage at each time point.

5. The observed transport between a channel and an open cavity

As discussed in § 3, flow disturbances such as the ones in figures 5 and 6 result in the formation of lobes at the downstream corner of the cavity. Figure 13 shows a sequence of experimental images illustrating one cycle of lobe formation. Perturbations cause dye passing over the downstream corner of the cavity to form a pair of lobes. One lobe plunges into the cavity and a companion lobe (of the same area) is simultaneously ejected from the cavity into the flow channel. The material leaving the cavity stays close to the channel wall and quickly leaves the imaging area.

Two primary measures of transport enhancement are lobe size and rate of lobe

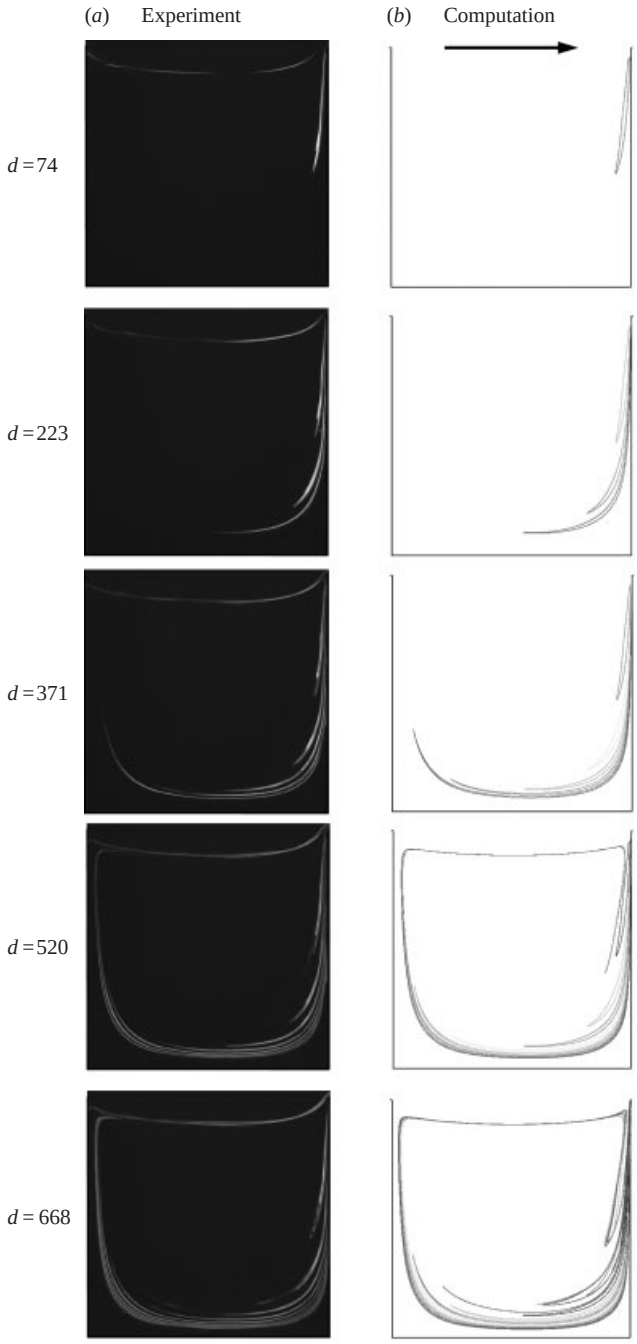

FIGURE 14. Length stretch and area coverage increase dramatically after the dyed material returns to the turnstile region. Also, note the agreement between the experimental dye advection results (*a*) and the numerical model (*b*). *d* is the linear cylinder displacement divided by the cavity width (T-mode, $Re = 19.26$, $ReSr = 0.26$).

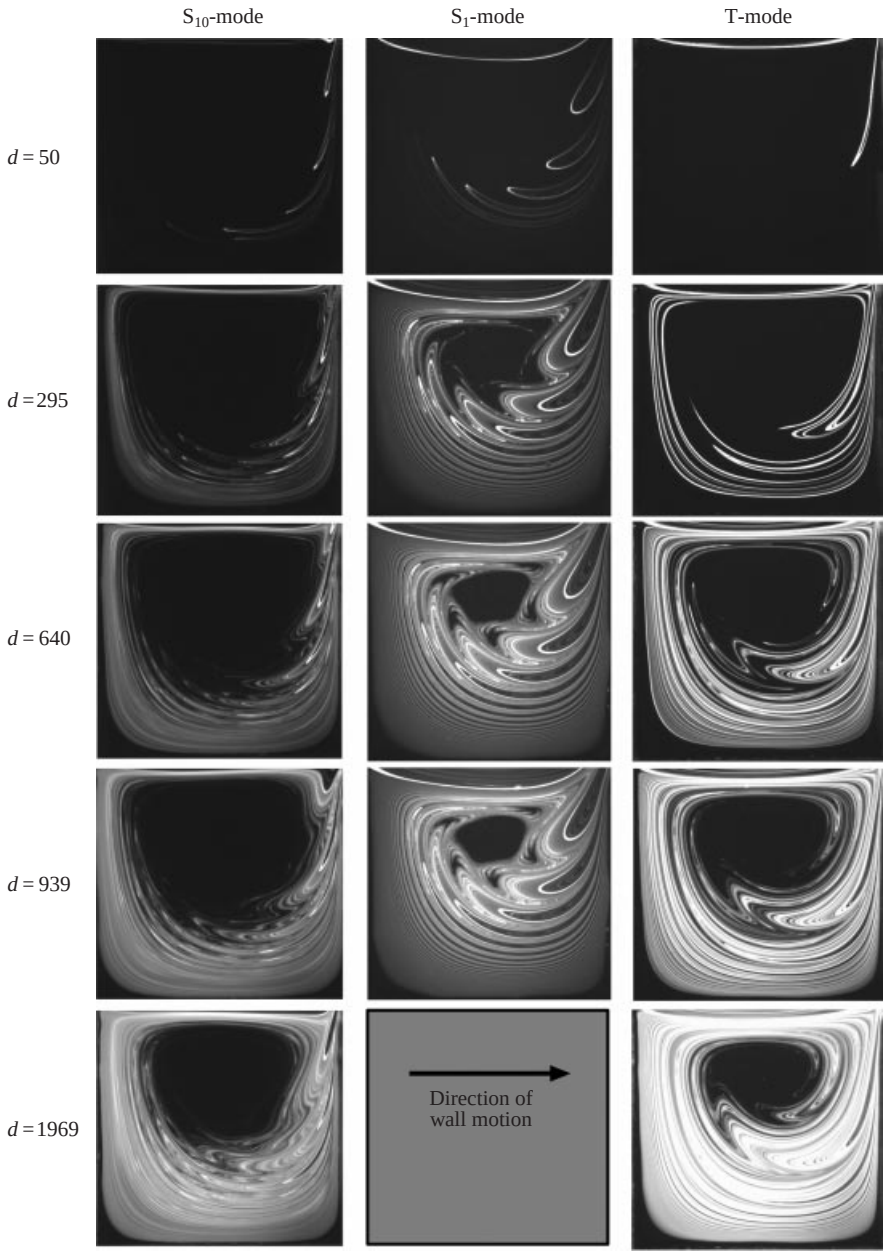

FIGURE 15. Efficiencies of the various modes of operation. The rate of area coverage is highest for the S_1 system. The final area coverage for the T system is the same as that of the S_1 system, but the T modification requires twice the energy input. The experimental conditions are as follows: T experiment – $Re = 62.0$, $ReSr = 1.26$; S_{10} experiment – $Re = 31.0$, $ReSr = 31.3$; S_1 experiment – $Re = 31.0$, $ReSr = 3.09$. The Reynolds number for the T-mode is chosen such that the average Reynolds number is the same for all three cases.

formation. The product of these two quantities corresponds to the transport rate of the turnstile. We determine the entrained lobe size $\mu(L_{ch,ca})$, abbreviated as $\mu(E)$, from digital images such as those in figure 13. This is done by determining the portion of pixels contained within a digital outline of the lobe which lies beneath the

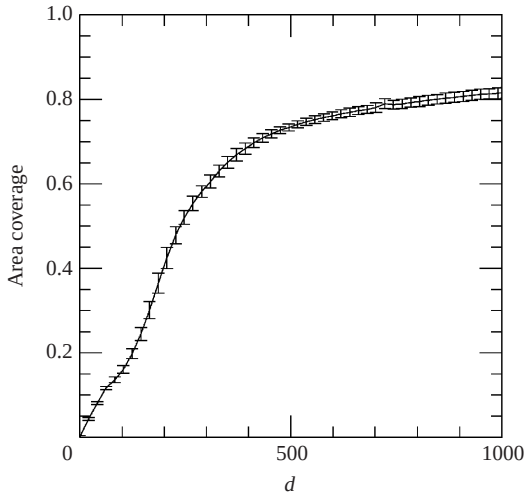

FIGURE 16. Area coverage as a function of dimensionless wall displacement d. Area coverage values are normalized to the area of the cavity beneath the seperatrix. Results are shown for four separate mixing experiments and the error bars represent two standard deviations in the data (S_1-mode, $Re = 31$, $ReSr = 2.71$, $H/W = 1.05$).

boundary curve $\mathscr{B}$ (see § 3). The location of $\mathscr{B}$ is estimated from the beginning of a lobe formation cycle, e.g. figures 13(a) or (k). The flux of material into the cavity ϕ is defined as lobe size divided by the displacement of the cylinder during the lobe formation event. This definition yields an average value for the flux based on the energy input into the system. We report all results in terms of the non-dimensional variables: therefore, lobe size $\mu(E)$ is normalized with respect to the cavity area LW and the flux function ϕ is normalized to the cavity width W.

Figure 14 shows a comparison between computation and experiment exhibiting repeated lobe formation events in the T-mode. Lobes roughly outline the more complicated portions of the unstable manifold of the upstream parabolic point (see figure 8). We show later that this process leads to an exponential stretch rate of lobe material. Representative examples from the spatially periodic (S_1- and S_{10}-modes) and transient (T-mode) experiments are shown in figure 15, each with the same (average) Reynolds number (but varying Reynolds–Strouhal number). The rate of area coverage and the maximum area coverage are highest for the S_1 modification. There is also considerable transport in the T-mode in spite of the fact that the instantaneous streamline portraits change very little during a flow cycle. The T and S_1 modifications both outperform the (higher frequency) S_{10} experiment. The next two sections address the dependence of transport rates on the forcing frequency, i.e. $ReSr$, for the S_N-mode and T-mode.

Typical experimental results for the area coverage of the cavity are shown in figure 16. The initial rate of area coverage is roughly linear, and then goes to zero as the maximum area coverage for a given Re–$ReSr$ is attained. The eventual decrease in the rate of area coverage occurs because the presence of residual KAM surfaces prevents complete coverage of the cavity interior. Thus, the 'mixing' region R_{mix} is defined as the region of the cavity below $\mathscr{B}$ minus all regions isolated by KAM tori. For experimental purposes, we define R_{mix} as the size of the mixing region after 100 flow perturbations. The results of figure 16 correspond to four separate runs and show the repeatability of this type of experiment.

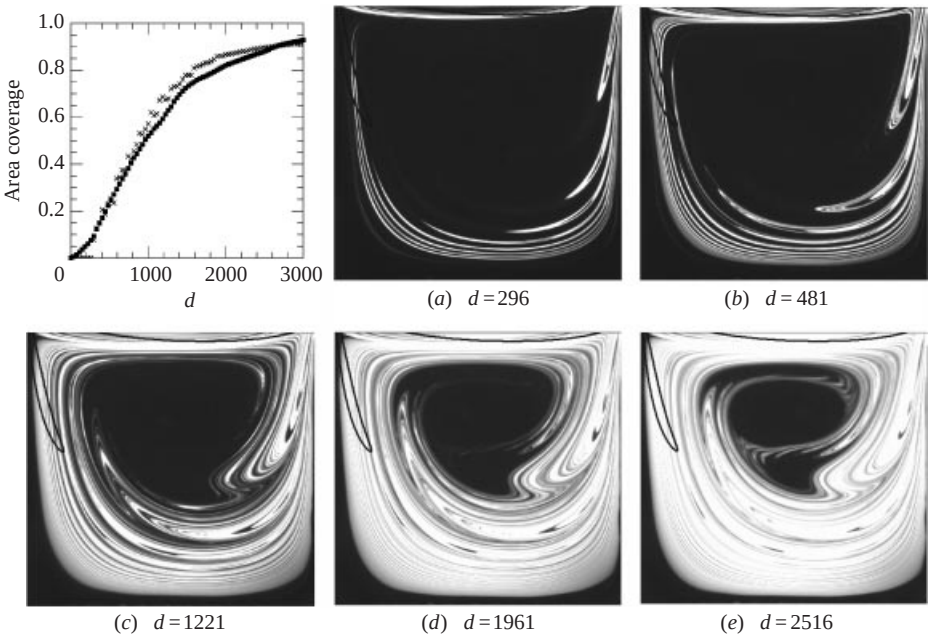

FIGURE 17. (*a*)–(*e*) Overlays of the detraining turnstile lobe ($L_{ca,ch}$) (in black) onto experimental dye advection results. The plot shows that the fractional area coverage of $L_{ca,ch}$ (×) is comparable to that of the mixing region (■) throughout the experiment. Note that we normalize the dye coverage to the area of the mixing region in this comparison only (T-mode, $Re = 46.5$, $ReSr = 1.26$).

We now note a possible relation between the fractional area coverage of the detraining turnstile lobe ($L_{ca,ch}$) and that of the cavity. An overlay of $L_{ca,ch}$ onto experimental images for the same *Re*–*ReSr* allows us to simultaneously observe the area coverage of the cavity and of $L_{ca,ch}$ (figure 17). The plot shows that the fractional area coverage of the turnstile mirrors that of the mixing region. Further investigation of this observation seems warranted. Next, we present more detailed results taken from experiments and computations of the open cavity flow.

6. S_N-mode enhancement: spatially varying boundary forcing

In this section we explore the effect of a spatially varying boundary on fluid exchange into an open cavity. The characteristic time T is the time between rod passages, i.e. $T = (Nv_{max})^{-1}$. Substituting for T in equation (2.6) yields

$$ReSr = \frac{W^2 N v_{max}}{\nu}. \tag{6.1}$$

We show experimental results for $7.74 \leqslant Re \leqslant 46.5$ and $0.52 \leqslant ReSr \leqslant 12.55$.

We perform two classes of experiments in order to investigate the effect of the two inertial terms in the equations of motion (2.3). First, by reducing the speed of the boundary proportionately as we increase N, Re decreases while $ReSr$ remains constant. This decreases the wavelength of the disturbance while keeping the wave speed constant. Second, increasing N while keeping v_{max} constant increases $ReSr$ while Re remains constant. The system size, as constructed, however, does not allow for a broad enough range of $ReSr$ (Re fixed) to fully explore the frequency dependence

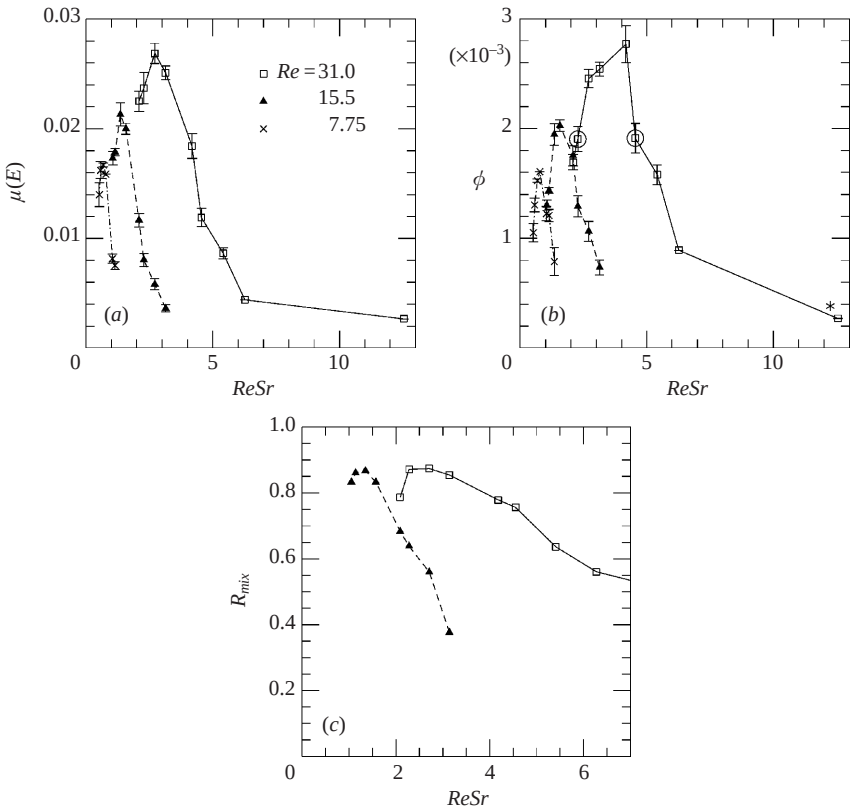

FIGURE 18. Experimental data summarizing (*a*) the dimensionless lobe size, (*b*) the flux, and (*c*) the size of the mixing region versus forcing frequency for the S_N-mode. Each of these variables exhibits a maximum as *ReSr* increases. Data are measured at three separate time points during an experiment, typically after 10, 30, and 50 perturbations. Each data point represents an average of these values from 2–3 separate experiments.

of the transport. Therefore, we isometrically scale down the system to increase the *Re*–*ReSr* parameter space.

Figure 18 summarizes the experimental results for the size of the lobe formed ($\mu(E)$), the flux of material into the cavity (ϕ), and the size of the mixing region (R_{mix}). For *Re* fixed, a curve with one maximum describes the variation of all three of these variables with frequency. For *ReSr* fixed, an increase in the Reynolds number results in increases in $\mu(E)$, ϕ, and R_{mix} over the entire range studied. Experimental results for global transport are shown in figure 19. Figure 19(*a*) shows that the total area coverage and flux increase as the Reynolds number increases (*ReSr* fixed). Figure 19(*b*) shows the progression of area coverage for varying *ReSr* (*Re* fixed). Two of the curves initially overlap because they have similar flux values (the circled data points in figure 18*b*); they eventually separate because the lobe size and size of the mixing region differ.

Increases in *ReSr* eventually lead to decreases in the frequency of lobe formation. In fact, no lobes form for *ReSr* high enough. One lobe forms for each rod that passes by the cavity in most of the experiments shown in figure 18. However, there is a reduction in the rate of lobe formation for the data in figure 18 marked with an asterisk (*), where only one lobe forms for every fourth rod that passes by the cavity. This

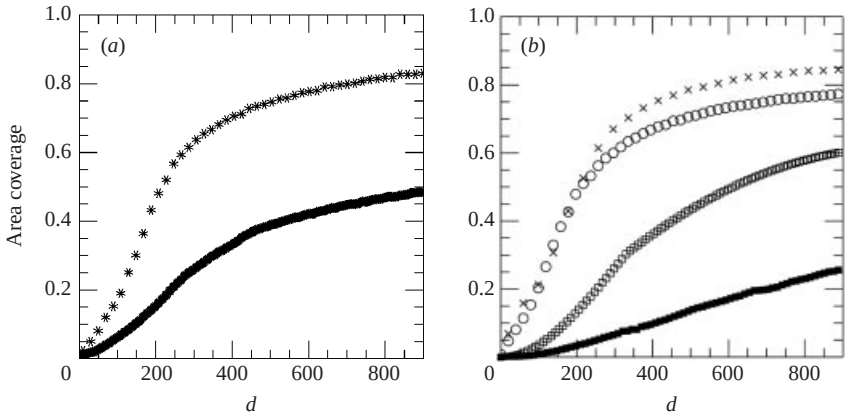

FIGURE 19. (*a*) Area coverage and transport rate increase as inertial effects increase ($ReSr = 3.14$ and $Re = 15.5$ (●), $Re = 31.0$ (∗)). (*b*) The progression of the area coverage is initially similar for the circled experimental flux values in figure 18(*b*). The rate of area coverage and total area coverage decrease as $ReSr$ increases for values of $ReSr$ beyond the maximum flux ($Re = 31.0$ and $ReSr = 2.28$ (×), $ReSr = \Omega.56$ (○), $ReSr = 6.27$ (□), $ReSr = 12.55$ (■)).

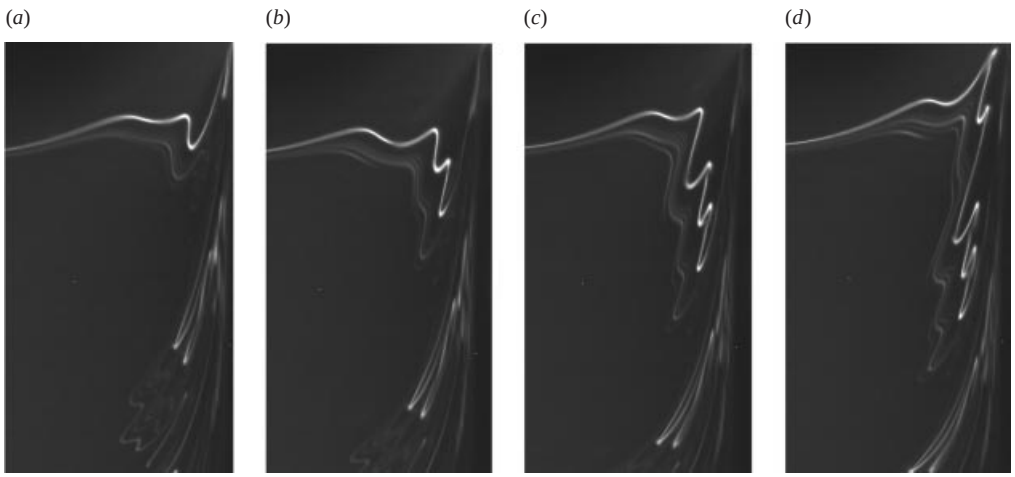

FIGURE 20. In this experiment, the edge of the forming lobe passes the downstream corner of the cavity only after four rods have passed ($Re = 15.5$, $ReSr = 15.7$). This new lobe shape signals a dramatic change in the manifold structure in the region of p_d. Images are shown for (*a*) $t = 0$ s, (*b*) $t = 0.8$ s, (*c*) $t = 1.6$ s, and (*d*) $t = 2.4$ s. The fainter dye lines are from earlier lobes that have had time to cycle back to the turnstile region.

reduction is accompanied by a dramatic change in lobe shape, an example of which is shown in figure 20. In general, the maximum splitting distance between stable and unstable manifolds becomes exponentially small when the forcing frequency becomes large.

We conclude this section by pointing out the changes in transport that occur for cavities containing more than one recirculating region in the main cavity space. Perturbing a flow such as the one shown in figure 1(*b*) typically results in only the upper flow cell containing dye from the channel. This is because the circulation amplitude in secondary flow cells decreases approximately a thousand-fold for each cell added to a deep cavity (Moffatt 1964). Even so, flow perturbations can cause

separation of the stable and unstable manifolds of the separatrix between the upper and lower flow cells. The turnstile between the upper and lower cells is located near the 'upstream' wall of the cavity however, as the flow direction is reversed for the lower separatrix (figure 21). A close-up of the upper turnstile region shows that some of the undyed portions of the upper flow cell are filled by material from below (figure 22). Therefore, the tangles of the two flow cells are intertwined by the S_1 perturbation. This also creates a connection between the secondary flow cell and the flow in the channel. Although we can determine the transport rate between these regions from experiments such as the one shown in figure 21, we do not consider this issue further here.

7. T-mode enhancement: purely transient forcing

In this section, we examine the effect of *Re* and *ReSr* on transport using transient forcing. As shown in figure 6, the separatrix is nearly unaffected during a single sawtooth cycle: streamlines at subsequent times are almost indistinguishable, even from those of the steady-state case. Despite this, there is significant transport between the cavity and channel.

The characteristic time T in the Strouhal number is v_{max}/a in the T-mode, and we have for the Reynolds–Strouhal combination

$$ReSr = \frac{W^2}{\nu}\frac{a}{v_{max}}. \tag{7.1}$$

We show experimental and computational results for $12 \leqslant Re \leqslant 93$ and $0.26 \leqslant ReSr \leqslant 5.02$.

We isolate the effect of the Reynolds number by varying v_{max} while keeping a/v_{max} constant, whereas we isolate the effect of the Reynolds–Strouhal term by varying the acceleration while keeping v_{max} constant. Figure 23 summarizes the experimental results for lobe size ($\mu(E)$), flux (ϕ), and mixing region size (R_{mix}). Each of these curves exhibits a maximum value for a given Reynolds number, and as seen in the S_N-mode, an increase in the Reynolds number results in increases in $\mu(E)$, ϕ, and R_{mix}. The frequency of lobe formation is once per sawtooth period for all reported values of *Re*–*ReSr*.

Figure 24 summarizes the experimental area coverage results for various values of *Re* and *ReSr*. For the case of fixed *ReSr* (figure 24*a*), the rate of area coverage and maximum area coverage increase with *Re*. As seen in the S_N-mode, the rate of area coverage is initially comparable for *Re*–*ReSr* pairs with similar fluxes (figure 24*b*). The curves separate because the mixing regions differ for the two experiments. The curve for the lowest *ReSr* value illustrates how the maximum area coverage may be higher even though the flux of material into the cavity is comparatively lower.

Figure 25 shows how the angle at which the lobe enters the cavity (measured relative to the cavity wall) decreases as *ReSr* decreases. This reflects the lobe following the steady-state streamlines more closely in the vicinity of the parabolic point, suggesting that transport is approaching the adiabatic limit, especially when $ReSr < 1$. This result is similar to the adiabatic chaos examined by Jana, Metcalfe & Ottino (1994) (especially their figure 31) for a hyperbolic point in a bounded flow, reinforcing the fact that transport near parabolic fixed points can display behaviour quite similar to that near a hyperbolic saddle. Also note how the dye line in the channel has not yet passed the downstream corner of the cavity in figure 25(*a*). The value of $\hat{t}$ (defined in figure 6) at which the leading edge of the entraining lobe sweeps downstream

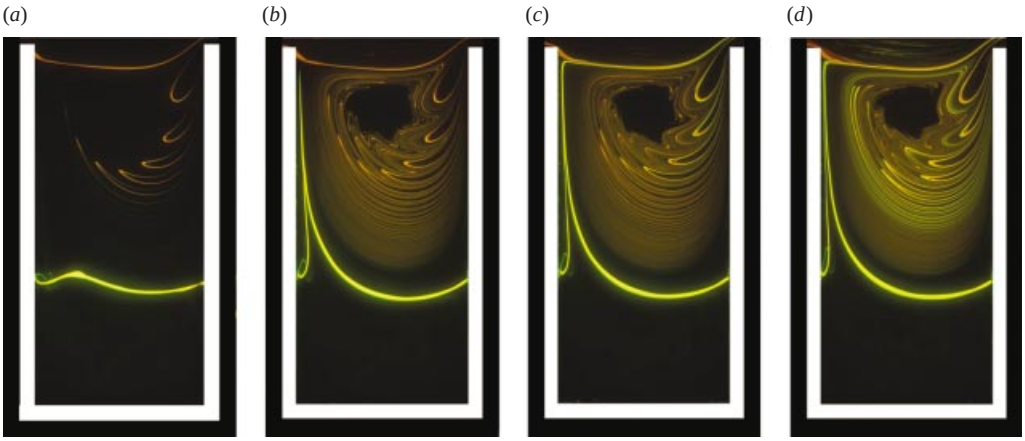

FIGURE 21. The unstable manifold of the lower flow cell (green dye) partially fills the empty portions of the primary flow cell (red dye). This is characteristic of perturbed transport in deep cavities. We approximate the separatrix between the two flow cells by injecting a line of green dye deep in the cavity before the experiment begins. Experimental conditions: S_1, $Re = 25.0$, $ReSr = 2.5$. (*a*) $d = 99$, (*b*) $d = 494$, (*c*) $d = 513$, (*d*) $d = 632$.

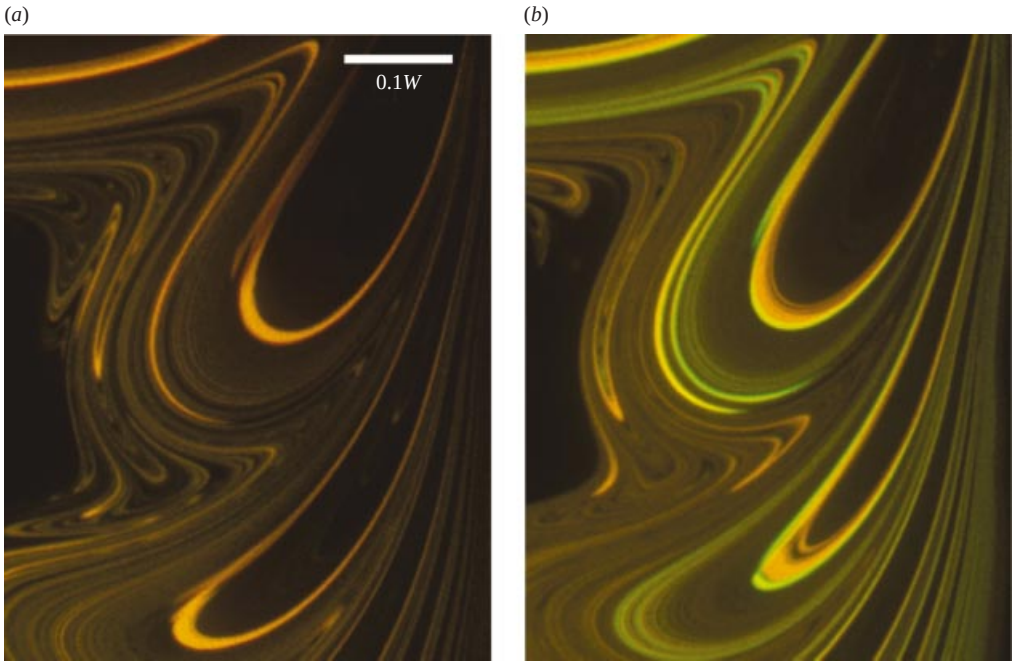

FIGURE 22. Closer inspection of images (*b*) and (*d*) from figure 21 reveals the fine structure of the flow in the turnstile region. Note how the green dye fills the voids between striations of red dye clearly illustrating the interconnection of the upper and lower flow cells. The green dye present in the flow channel also illustrates the connection between the fluid in the lower flow cell and the flow channel. (*a*) $d = 494$, (*b*) $d = 632$.

increases as $ReSr$ increases, i.e. as the cycle time decreases. The characteristic time for the diffusion of momentum across the channel is $h^2/\nu = 6.4\,\mathrm{s}$, which is very close to the cycle time of 10 s for the experiment in figure 25(*a*).

A Poincaré map of the perturbed flow shows the changes in the asymptotic flow

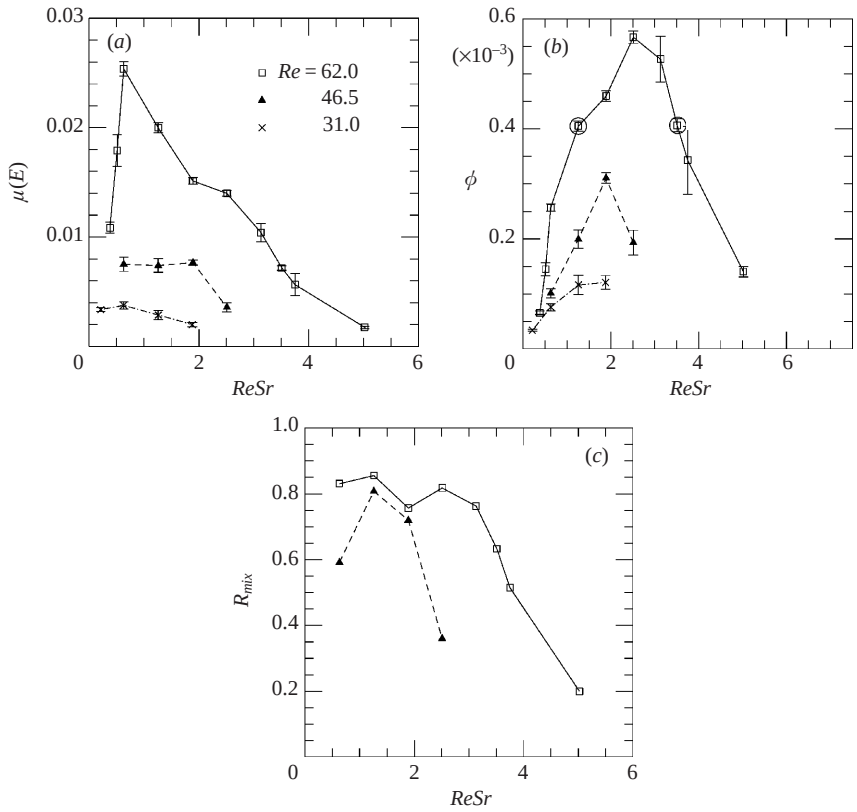

FIGURE 23. Experimental data summarizing (*a*) the dimensionless lobe size, (*b*) the flux, and (*c*) the size of the mixing region versus forcing frequency for the T-mode. The maximum in the data is not as clearly pronounced as the Reynolds number decreases. See figure 18 for a description of the data collection method.

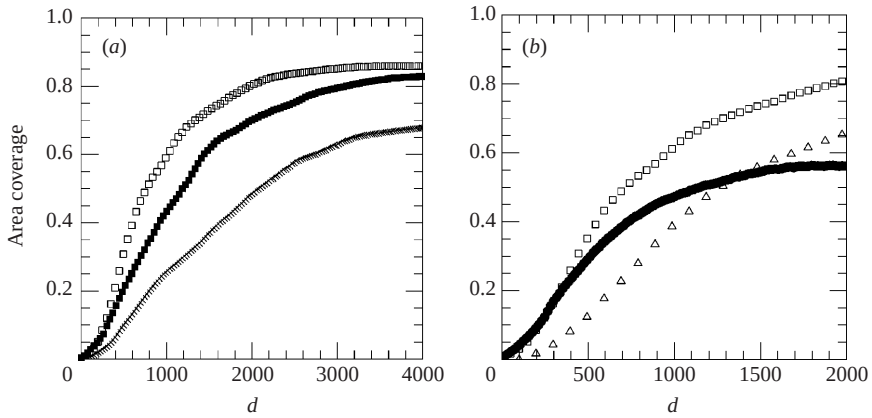

FIGURE 24. (*a*) Increasing *Re* at fixed $ReSr = 1.26$ increases the global transport rate as well as the total area coverage ($Re = 31.0$ (×), $Re = 46.5$ (■), $Re = 62.0$ (□)). (*b*) The rate of area coverage is initially similar for the circled data points in figure 23(*b*), the two curves eventually separate as the mixing region for $ReSr = 3.51$ becomes filled at fixed $Re = 62.0$. ($ReSr = 0.63$ (△), $ReSr = 1.26$ (□), $ReSr = 3.51$ (●)).

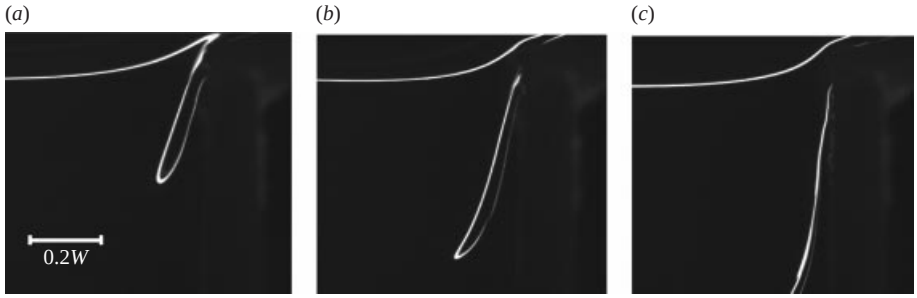

FIGURE 25. The length of a lobe at the end of one sawtooth period increases as $ReSr$ approaches the adiabatic limit. Lobe area decreases as $ReSr$ decreases, however. Experimental conditions: (*a*) $ReSr = 2.51$, (*b*) $ReSr = 1.26$, (*c*) $ReSr = 0.63$ ($Re = 62.0$).

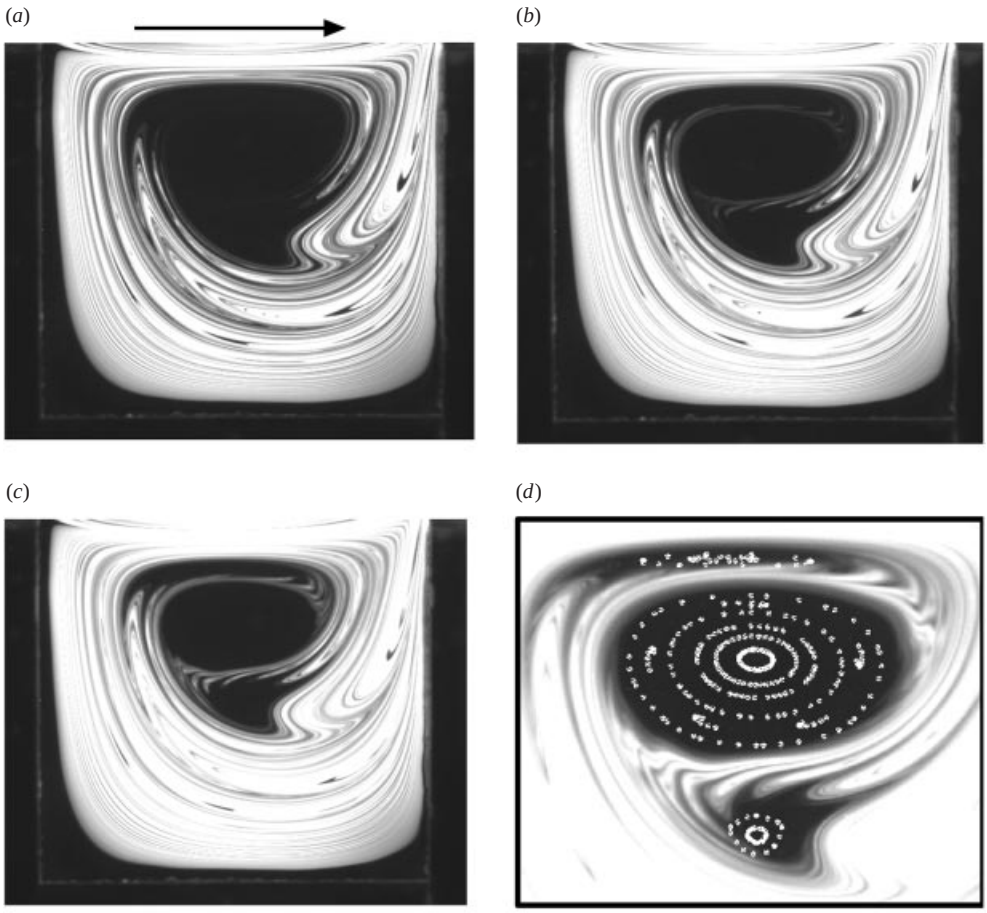

FIGURE 26. Creation of a period-2 island (*a–c*). (*d*) An overlay of the numerical results for the Poincaré map on the experimental data for $d = 3703$ (100 revolutions) shows excellent agreement between the two methods (T-mode, $Re = 46.5$, $ReSr = 1.26$).

structure as a function of system parameters. To generate such a map, we use an initial condition consisting of a line of 56 evenly spaced points spanning the region between the separatrix and the centre of the elliptic island. The points are advected for 100 sawtooth cycles. We record a dot for each particle after each period. Particles

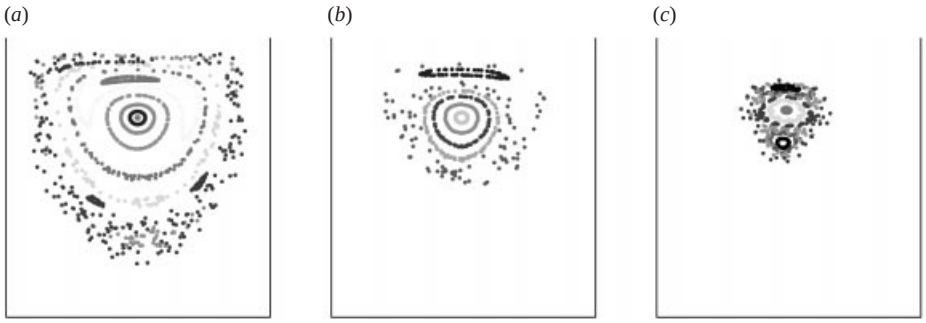

FIGURE 27. Poincaré sections for (*a*) $Re = 19.3$, (*b*) $Re = 41.2$, and (*c*) $Re = 92.9$. Eliminating all particles that leave the cavity (and their previous iterates) identifies the size of the core region (100 revolutions, $Sr = 0.014$).

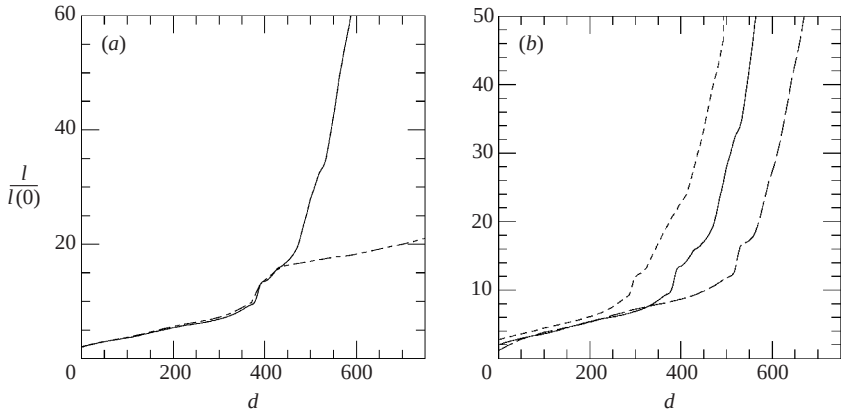

FIGURE 28. (*a*) Comparison of the length stretch of a lobe under the sawtooth advection ($Re = 19.26$ (——), $ReSr = 0.26$ and the same lobe in a steady field at the average velocity of the sawtooth protocol ($Re = 9.63$ (– - – - –)). (*b*) The length stretch of the lobe $L_{ch,ca}$ increases with Re ($Re = 12.84$ (— — —), $Re = 19.26$ (——), $Re = 25.67$ (- - -); $ReSr = 0.26$).

that leave the cavity have all their dots eliminated. As the number of flow periods becomes large, the remaining particles generate a Poincaré section. Figure 26 shows dye slowly filling the region around a large central island that is surrounded by a period-2 island chain. The numerical map is able to accurately resolve the long-time structure of the flow (figure 26*d*). Figure 27 shows how increasing the Reynolds number increases the size of the mixing region, and that isolated regions persist even at the highest Reynolds number studied.

We now narrow our focus from the overall structure of the flow to the advection of a single lobe in the cavity. Specifically, we use the numerical model to follow the length stretch of $L_{ch,ca}$, i.e. that portion of the unstable manifold that enters the cavity to form the entrained lobe. Tracking the length of the perimeter of a single lobe quantifies not only the stretching experienced by channel material upon entering the cavity, but also yields an estimate of how far the lobe has advected along the unstable manifold. Length stretch also gives some insight into the diffusion length that must be traversed by solutes trapped in the lamellar structure of the perturbed cavity flow. The length stretch of a material line is given by $l(d)/l(0)$, where $l(d)$ is the lobe length at displacement d of the cylinder and $l(0)$ is the initial length of $L_{ch,ca}$. The initial condition for each run is a set of 10 000 points distributed along that portion of the

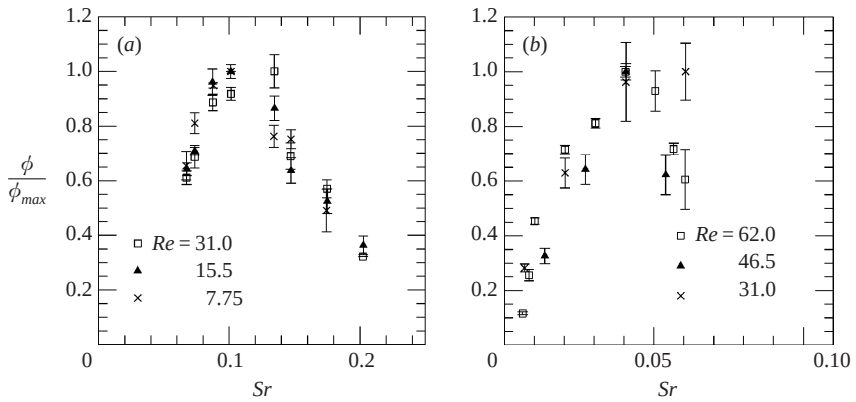

FIGURE 29. (*a*) The S_N-mode flux data of figure 18(*b*) collapse when scaled with the maximum flux value for each Reynolds number. The peak in the data occurs at $Sr \approx 0.1$. (*b*) The T-mode flux data (figure 23*b*) exhibits a characteristic frequency at $Sr \approx 0.04$.

separatrix that makes up $L_{ch,ca}$. This initial condition is determined separately for each *Re–ReSr* pair.

First, we compared the stretching of a lobe in the sawtooth flow to that in a steady flow at the average velocity of the sawtooth wave (figure 28*a*). After a lag period, material advecting in the T-mode flow experiences a sustained increase in length stretch over that of the steady flow. The sudden increase in the length stretch observed in the steady flow at $d \approx 375$ is due to the lobe advecting near the separatrix, where the velocity is highest compared to the rest of the cavity. The duration of the period of slow stretching decreases as the Reynolds number increases (figure 28*b*). We verified that the stretch rate is indeed exponential, and that the exponential stretch rate increases with Reynolds number.

8. Summary and conclusions

We have illustrated two approaches for enhancing transport in open cavity flows. Both methods increase the rate of fluid exchange between a channel and an open cavity over that of diffusion alone. The trends in transport depend on the flow modification, as well as the frequency and amplitude of the forcing. The frequency dependence exhibits a maximum: the flux increases for low frequencies and then decreases when *ReSr* exceeds a critical value. The S_N-mode flux data in figure 18(*b*) collapse when scaled with the maximum flux value and plotted versus Strouhal number (figure 29*a*), the optimum occurring at $Sr \approx 0.1$. The T-mode flux data also exhibit a characteristic frequency (figure 29*b*) at which the flux of material into the cavity is maximized ($Sr \approx 0.04$), but there is more scatter. In both cases, the transport increases with the amplitude of the forcing for the entire range tested. Another noteworthy result is that in spite of the stark contrast of the (instantaneous) streamline plots for the two flows (see figures 5 and 6), the T and S_{10} systems produce similar transport.

We may qualitatively interpret the local transport in the T- and S_N-modes through a Fourier analysis of the work done on the fluid by a transient velocity pulse. In the Appendix we show that the fraction of energy in a transient pulse that is not attenuated by viscosity is

$$P_C = Cv\frac{Re}{Sr}M(ReSr), \tag{8.1}$$

where C is a constant and $M(ReSr)$ is an increasing function of $ReSr$; both C and $M(ReSr)$ depend on the exact waveform of the forcing. Since equation (8.1) refers to a single cycle of the flow we expect $\phi \sim P_C$, i.e. P_C is as a predictive measure of the flux of material into the cavity through the turnstile. The theory captures the qualitative features of the flux function for the spatially dependent mode and transient modifications. The theory predicts that the flux increases linearly for low frequencies, and decays as $1/Sr$ for large frequencies.

There are several potential uses of the flow modifications presented here. Some are eminently practical. For example, Horner *et al.* (1998) recently studied mass transport in a perfusion bioreactor for the culture of human tissue cells. This bioreactor consists of a flow channel with a series of open cavities at the chamber bottom where cells grow. Channel flow constantly supplies cells with nutrients and removes waste products that inhibit growth. The use of a pulsatile inlet flow may enhance transport in these types of chambers. Lobe formation would directly supply channel material to the cells in the cavity and simultaneously remove cellular waste products that can inhibit growth. Indeed, pulsatile flow has already been shown to enhance cell output in a tubular bioreactor containing baffles (Harrison & Mackley 1992). Another unexplored area of the use of T-type transport enhancement could be in microfluidic mixing devices. A more theoretical reason to study open chaotic flows is that open flows behave differently than closed flows, particularly with regard to the effects of advection on autocatalytic chemical activity (see Tél *et al.* 2000 for a review of this emerging area).

A primary output of this work is general prescriptions for enhancing heat/mass transport. An order of magnitude estimate of the time required to diffuse through a stagnant layer of length H is H^2/D, where D is the diffusivity of the solute of interest. Steady recirculation in the cavity may result in significant transport enhancement, the so-called 'stirring' effect (Chilukuri & Middleman 1983). Enhancement typically increases with Péclet number, $Pe = UH/D$. Assuming $D \approx 10^{-5}\,\mathrm{cm^2\,s^{-1}}$ and a characteristic velocity in the cavity $U \approx 10^{-3}\,\mathrm{cm\,s^{-1}}$, we would expect a 30% reduction in the cleaning time due to the introduction of steady recirculation in the cavity (Chilukuri & Middleman 1983, figure 3 in their paper); this results in an approximate cleaning time of $0.7H^2/D = 1.4 \times 10^6$ s. A typical duration of one of our open cavity experiments is 10^3 s, a three orders of magnitude increase in the transport rate.

The work supported in part by the Department of Energy, Division of Basic Energy Sciences (J. M. O.) and ONR Grant No. N00014-97-1-0071 (S. W.).

Appendix. Heuristic analysis of transient forcing on the generation of lobes in open cavities

Here we derive a functional form for the energy available for lobe formation in terms of system parameters. This estimate is derived from the power spectrum of the velocity profile of the boundary forcing. The potential effect of the external time-dependent forcing is more easily seen in terms of the vorticity ω. In two dimensions, ω is governed by

$$ReSr\frac{\partial \omega}{\partial t} + Re\boldsymbol{u}\cdot\nabla\omega = \nabla^2\omega. \tag{A 1}$$

As a first approximation, we neglect convection. This simplifies equation (A 1) to

$$ReSr\frac{\partial \omega}{\partial t} = \nabla^2\omega. \tag{A 2}$$

Equation (A 2) indicates that any time-varying forcing will generate vorticity in the flow. In the open cavity flow, vorticity generated at the moving boundary wall destabilizes the downstream attachment point of the separatrix to generate a lobe pair.

When is a disturbance large enough to potentially initiate significant transport and how does the subsequent transport depend on the parameters of the experiment? Equation (A 2) suggests that disturbances with frequencies small compared to $ReSr$ will be attenuated by inertia while comparatively large frequencies will be unattenuated. Somewhat arbitrarily we can determine a critical frequency by setting

$$ReSr = \left(\frac{W^2}{\nu}\right) f_{crit} \sim 1, \tag{A 3}$$

where $f_{crit} = 1/T$ for a waveform of period T. This is not to say that $ReSr < 1$ is a cut-off frequency, but it does allow us to calculate a functional dependence by breaking up the disturbance into attenuated and unattenuated parts. For glycerin containing 10% H_2O, $\nu = 1.58\,\mathrm{cm^2\,s^{-1}}$ and taking $W = 4.445\,\mathrm{cm}$, $f_{crit} \approx 0.08\,\mathrm{Hz}$. Thus, forcing producing frequencies much above 0.08 Hz will make the time-derivative acceleration term have a larger effect. This is an acceleration effect different from a high-Re effect; in fact if Re is made smaller by lowering v_{max}, there is no effect on the product $ReSr$.

To quantify these considerations, first notice that the total power P_T (in the Fourier sense) in a velocity pulse with physically reasonable properties is proportional to the maximum velocity in the pulse v_{max} squared times the duration of the pulse T. Using the definitions of Re and Sr, the total power can be written as

$$P_T = C\nu\frac{Re}{Sr}, \tag{A 4}$$

where ν is the kinematic viscosity and gives the correct units for power for a velocity pulse. The dimensionless constant C depends on the waveform of the pulse and is calculated from $\int |g(t)|^2 \mathrm{d}t$, where $g(t)$ is the pulse waveform.

How much of the pulse energy is available to excite unattenuated disturbances in the flow? Any function $g(t)$ of transient forcing can be decomposed into its Fourier transform. Forcing frequencies f such that $ReSr \ll 1$ mean the $\partial\omega/\partial t$ term in equation (A 2) is small, while those frequencies such that $ReSr \gg 1$ mean the $\partial\omega/\partial t$ term is large during their existence. A convenient measure of the likely effect of a given forcing is then the ratio M of energy in frequencies such that $ReSr \geqslant 1$ to the total energy in the forcing,

$$M(ReSr) = \frac{\displaystyle\int_{\bar{f}}^{\infty} |G(f)|^2 \mathrm{d}f}{\displaystyle\int_{0}^{\infty} |G(f)|^2 \mathrm{d}f}, \tag{A 5}$$

where $|\,G(f)\,|^2$ is the power spectrum of $g(t)$ and

$$G(f) = \int_{-\infty}^{\infty} g(t)\mathrm{e}^{\mathrm{i}2\pi f t}\mathrm{d}t \tag{A 6}$$

is the Fourier transform of $g(t)$. The integration limit $\bar{f} = \nu/h^2$ is a natural damping frequency dependent on the fluid and system geometry. The definition of $ReSr$ can be expressed as $ReSr = f/\bar{f}$.

The total energy going into disturbing the steady fluid motion is $P_C = P_T M$.

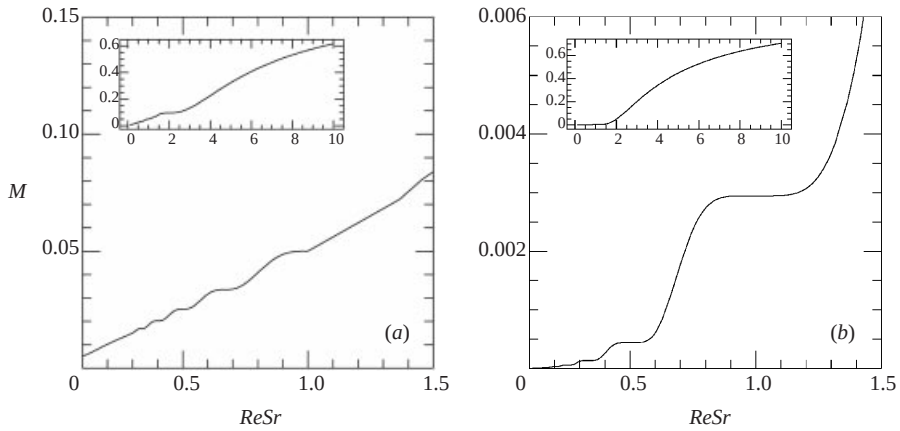

FIGURE 30. Fraction of energy from a transient velocity pulse available for lobe formation as a function of $ReSr$ for (a) a square pulse and (b) a triangular pulse.

Calculating all this, however, is redundant as the integral of $g(t)^2$ equals the integral of $G(f)^2$ by Parseval's theorem. So

$$P_C = \int_{\bar{f}}^{\infty} |G(f)|^2 \mathrm{d}f. \tag{A 7}$$

For $P_C \neq 0$ we expect to generate some transport because the acceleration term acts as a transient perturbation on the steady-state flow. As P_C, or M, tends towards zero, we expect the same results as for adiabatic, or infinitely slowly applied, perturbations.

As all transient wave forms $g(t)$ are effectively convolved with a square pulse, the well known 'leakage' of energy to higher frequencies with a square pulse is an important generator of transient chaos. For a square pulse that turns on at $-T$ and turns off at T, $C = 2$ and

$$M(ReSr) = 2 \int_{2/ReSr}^{\infty} \mathrm{sinc}^2(\pi z)\mathrm{d}z, \tag{A 8}$$

where $\mathrm{sinc}(\pi z)z \equiv \sin(\pi z)/(\pi z)$ and z is a dummy integration variable. For an appropriate scaling of the characteristic time T, the forcing by the cylindrical rods can be approximated as a series of square waves. For our experiments we also chose to use a triangular pulse in order to more easily vary $ReSr$. For a triangular pulse that starts at $-T$ and finishes at T, $C = 2/3$ and

$$M(ReSr) = 3 \int_{1/ReSr}^{\infty} \mathrm{sinc}^4(\pi z)\mathrm{d}z. \tag{A 9}$$

Figure 30 shows $M(ReSr)$ for (a) the square pulse and (b) the triangular pulse as a function of $ReSr$.

To summarize, the fraction of energy per transient pulse available to generate lobe pairs is

$$P_C = Cv\frac{Re}{Sr}M(ReSr). \tag{A 10}$$

P_C is a function of both the ratio of Re and Sr and their product. Re/Sr is the overall amplitude per pulse and $ReSr$ sets the fraction of that energy available to

cause appreciable fluid acceleration. Also note that P_C is proportional to $1/Sr$ for large forcing frequencies.

From this analysis we expect that the flux of material into the cavity is proportional to P_C, and this gives the functional dependence of the transport rate on the fluid parameters. In spite of neglecting the convection term, equation (A 10) agrees qualitatively with the experimental results; the experimental and theoretical curves have similar shapes. More physics must be included before this analysis is a quantitative predictor of the flux function.

REFERENCES

Alkire, R. & Verhoff, M. 1994 Electrochemical reaction engineering in materials processing. *Chem. Engng Sci.* **49**, 4085–4093.

Casasayas, J., Fontich, E. & Nunes, A. 1992 Invariant manifolds for a class of parabolic points. *Nonlinearity* **5**, 1193–1210.

Chilukuri, R. & Middleman, S. 1983 Circulation, diffusion, and reaction within a liquid trapped in a cavity. *Chem. Engng Commun.* **22**, 127–138.

Fang, L. C., Nicolaou, D. & Cleaver, J. W. 1999 Transient removal of a contaminated fluid from a cavity. *Intl J. Heat Mass Transfer*, **20**, 605–613.

Fontich, E. 1999 Stable curves asymptotic to a degenerate fixed point. *Nonlin. Anal.* **35**, 711–733.

Frankel, G. S. 1998 Pitting corrosion of metals: a review of critical factors. *J. Electrochem. Soc.* **145**, 2186–2198.

Garrison, B. & Rogers, C. 1994 An experimental study of enhanced fluid transfer mechanism between a channel and a cavity. *Phys. Fluids* **6**, 421-423.

Ghaddar, N. K., Korczak, K. Z., Mikic, B. B. & Patera, A. T. 1986 Numerical investigation of incompressible flow in grooved channels. Part 1. Stability and self-sustained oscillations. *J. Fluid Mech.* **163**, 99–127.

Ghosh, S., Leonard, A. & Wiggins, S. 1998 Diffusion of a passive scalar from a no-slip boundary into a two-dimensional chaotic advection field. *J. Fluid Mech.* **372**, 119–163.

Haller, G. & Poje, A. C. 1998 Finite time transport in aperiodic flows. *Physica* D **119**, 352–380.

Harrison, S. T. L. & Mackley, M. R. 1992 A pulsatile flow bioreactor. *Chem. Engng Sci.* **47**, 490–493.

Higdon, J. J. L. 1985 Stokes flow in arbitrary two-dimensional domains: shear flow over ridges and cavities. *J. Fluid Mech.* **159**, 195–226.

Horner, M., Miller, W. M., Ottino, J. M. & Papoutsakis, E. T. 1998 Transport in a grooved perfusion flat-bed bioreactor for cell therapy applications. *Biotech. Prog.* **14**, 689–698.

Howes, T. & Shardlow, P. J. 1997 Simulation of mixing in unsteady flow through a periodically obstructed channel. *Chem. Engng Sci.* **52**, 1215–1225.

Jana, S. C., Metcalfe, G. & Ottino, J. M. 1994 Experimental and computational studies of mixing in complex Stokes flows: the vortex mixing flow and multicellular cavity flows. *J. Fluid Mech.* **269**, 199–246.

Jana, S. C. & Ottino, J. M. 1992 Chaos-enhanced transport in cellular flows. *Phil. Trans. R. Soc. Lond.* A **338**, 519–532.

Mackay, R. S., Meiss, J. D. & Percival, I. C. 1984 Transport in Hamiltonian systems. *Physica* **13D**, 55–81.

Malhotra, N. & Wiggins, S. 1998 Geometric structures, lobe dynamics, and Lagrangian transport in flows with aperiodic time dependence, with applications to Rossby wave flow. *J. Nonlin. Sci.* **8**, 401–456.

McGehee, R. 1973 A stable manifold theorem for degenerate fixed points with applications to celestial mechanics. *J. Diffl Equat.* **14**, 70–88.

Meinders, E. R., Meer, T. H. V. D. & Hanjalic, K. 1998 Local convective heat transfer from an array of wall-mounted cubes. *Intl J. Heat Mass Transfer* **41**, 335–346.

Miller, P. D., Jones, C. K. R. T., Rogerson, A. M. & Pratt, L. J. 1997 Quantifying transport in numerically generated velocity fields. *Physica* D **110**, 105–112.

Miner, C. S. & Dalton, N. N. (Eds.) 1953 *Glycerol.* Reinhold Publishing Corporation.

Moffatt, H. K. 1964 Viscous and resistive eddies near a sharp corner. *J. Fluid Mech.* **18**, 1–18.

Recktenwald, A., Lücke, M. & Müller, H. M. 1993 Taylor vortex formation in axial through-flow: linear and weakly nonlinear analysis. *Phys. Rev.* E **48**, 4444–4453.

Roberts, E. P. L. & Mackley, M. R. 1995 The simulation of stretch rates for the quantitative prediction and mapping of mixing within a channel flow. *Chem. Engng Sci.* **50**, 3727–3746.

Rom-Kedar, V., Leonard, A. & Wiggins, S. 1990 An analytical study of transport, mixing and chaos in an unsteady vortical flow. *J. Fluid Mech.* **214**, 347–394.

Rom-Kedar, V. & Poje, A. C. 1999 Universal properties of chaotic transport in the presence of diffusion. *Phys. Fluids* **11**, 2044–2057.

Shankar, P. N. & Deshpande, M. D. 2000 Fluid mechanics in the driven cavity. *Annu. Rev. Fluid Mech.* **32**, 93–136.

Shehata, A. K., Yang, J. D., West, A. C. & Modi, V. 1999 Effect of an unsteady external flow in mass transfer to cavities. *Intl J. Heat Mass Transfer* **42**, 673–683.

Solomon, T. H., Tomas, S. & Warner, J. L. 1998 Chaotic mixing of immiscible impurities in a two-dimensional flow. *Phys. Fluids* **10**, 342–350.

Tél, T., Károlyi, G., Péntek, Áron., Scheuring, I., Toroczkai, Z., Grebogi, C. & Kadtke, J. 2000 Chaotic advection, diffusion, and reactions in open flows. *Chaos* **10**, 89–98.

Tighe, S. & Middleman, S. 1985 An experimental study of convection-aided removal of a contaminant from a cavity in a surface. *Chem. Engng Commun.* **33**, 149–157.

Yuster, T. & Hackborn, W. W. 1997 On invariant manifolds attached to oscillating boundaries in Stokes flows. *Chaos* **7**, 769–776.